

Properties of $K^*(890)$ and $K^*(1400)$ Produced in K^-p Interactions at 4.1 and 5.5 GeV/c*

F. SCHWEINGRUBER†

Argonne National Laboratory, Argonne, Illinois

and

Northwestern University, Evanston, Illinois

AND

M. DERRICK, T. FIELDS,‡ DAVID GRIFFITHS,§ L. G. HYMAN, R. J. JABBUR,|| AND J. LOKEN

Argonne National Laboratory, Argonne, Illinois

AND

R. AMMAR, R. E. P. DAVIS, W. KROPAC, AND J. MOTT

Northwestern University, Evanston, Illinois

(Received 24 August 1967)

The results presented in this paper were obtained from an analysis of K^-p interactions in the 30-in. hydrogen bubble chamber at the Argonne ZGS using incident K^- beams of momenta 4.1 and 5.5 GeV/c. The $\bar{K}^0\pi N$ final states were studied extensively; the most prominent feature of these is production of the $K^*(890)$ and $K^*(1400)$ resonances. The $\bar{K}^0\pi^-\pi^+n$ final state was used to measure the branching ratio of the decay of the $K^*(1400)$ into $K^*(890)\pi$ and $K\rho$. Evidence for quasi-two-body production of $K^*(890)^-$ and $K^*(1400)^-$ is presented both from the two-prong events in which the positive track was identified as a proton, and from events where the \bar{K}^0 decay was observed. For final states with a missing neutron, a study of the missing-mass distributions proved that the kinematical fits to $K^-\pi^+n$ and $\bar{K}^0\pi^-\pi^+n$ final states could be used with confidence to study $K^*(890)^0$ and $K^*(1400)^0$ production. The $K^*(890)^0$ - production angular distribution and decay correlations are analyzed in the framework of the absorptive peripheral model. Vector exchange dominates the $K^*(890)^-$ production, whereas $K^*(890)^0$ is formed mainly via pseudoscalar exchange. An absorptive-peripheral-model calculation using the vector-meson coupling strengths to the nucleon given by relativistic $SU(6)$ gives a good fit to the $K^*(890)^0$ - density-matrix elements as a function of production angle, and gives a reasonable fit to the differential cross section. For the $K^*(1400)$ resonance, a mass and width of 1416 ± 8 and 107 ± 20 MeV are obtained. Decay branching ratios measured for this resonance of $K\pi:K^*\pi:K\rho$ of $1:(0.52 \pm 0.12):(0.26 \pm 0.16)$ are in agreement with those predicted from $SU(3)$ assuming the $K^*(1400)$ is a member of a 2^+ nonet. The absorptive peripheral model gives no reasonable fits to the $K^*(1400)$ production angular distributions. The $K^*(1400)^0$ - production and decay angular distributions suggest that the spin parity of the $K^*(1400)$ is 2^+ , but without many more events, or a better model for the production mechanism, we cannot make a decisive determination.

I. INTRODUCTION

HIGH-ENERGY K^-p interactions are studied using film from the 30-in. hydrogen bubble chamber at the Argonne ZGS. We have analyzed the two-prong-plus- V events and the two-prong events in the 90 000 pictures taken at 4.1 GeV/c and the 400 000 pictures taken at 5.5 GeV/c. In this paper we present a study of the quasi-two-body production of $K^*(890)$ and $K^*(1400)$ observed in the final states

$$K^-p \rightarrow \bar{K}^0\pi^-p \quad (1.1)$$

$$\rightarrow K^-\pi^+n \quad (1.2)$$

$$\rightarrow \bar{K}^0\pi^-\pi^0p \quad (1.3)$$

$$\rightarrow \bar{K}^0\pi^+\pi^-n. \quad (1.4)$$

Reaction (1.1) has been studied extensively at lower energies.^{1,2} $K^*(890)^-$ is produced copiously in this final state and the decay angular correlations interpreted using the absorptive peripheral model indicate that although both pseudoscalar and vector exchange occur in the $K^*(890)^-$ production process, the vector exchange is dominant. Jackson *et al.*³ have analyzed much of the data on this reaction and have found acceptable fits to the density-matrix elements but not to the energy dependence of the reaction cross section.

Although vector exchange for $K^*(890)^-$ production is indicated from the analysis of reaction (1.1), whether the exchanged particle is ρ , ω , or ϕ cannot be determined from this reaction alone since zero charge is exchanged. The isospin of the exchanged particle can be investi-

* Supported by the U. S. Atomic Energy Commission and National Science Foundation.

† This work forms part of a dissertation submitted to Northwestern University in partial fulfillment of the requirements for the Ph.D. degree.

‡ Also at Northwestern University, Evanston, Ill.

§ Now at Johns Hopkins University, Baltimore, Md.

|| Now at Physics Department, City College, City University of New York, New York, N. Y.

¹ R. Barloutaud, A. Leveque, C. Louedec, J. Meyer, P. Schlein, A. Verglas, J. Badier, M. Demoulin, J. Goldberg, B. P. Gregory, P. Krejbich, C. Pelletier, M. Ville, E. S. Gelsema, J. Hoggland, J. C. Kluyver, and A. G. Tenner, Phys. Letters **12**, 352 (1964).

² J. H. Friedman and R. R. Ross, Phys. Rev. Letters **16**, 485 (1966).

³ J. D. Jackson, J. T. Donohue, K. Gottfried, R. Keyser, and B. E. Y. Svensson, Phys. Rev. **139**, B428 (1965). J. T. Donohue, Ph.D. thesis, University of Illinois, 1967 (unpublished).

gated by comparison of this reaction with reaction (1.2) in which a charged particle must be exchanged. $K^*(890)^0$ production in reaction (1.2) has been studied at 3.0 GeV/c.⁴ The analysis showed that pseudoscalar exchange is dominant in production of $K^*(890)^0$. Information on the isospin of the vector meson exchanged in $K^*(890)^-$ production was obtained by comparing the vector-exchange contributions to the cross sections for $K^*(890)$ production in reactions (1.1) and (1.2). Pure $T=1$ (0) vector exchange for K^{*-} production would require that the cross section for K^{*0} production be 4 (0) times as large as the cross section for K^{*-} production. The observed ratio of the vector-exchange parts of the cross sections was 0.19 ± 0.13 . From this result, assuming the $\phi N\bar{N}$ coupling is negligible, one concludes that ω exchange is the dominant process in $K^*(890)^-$ production. Studies of K^+p and K^+n interactions at 2.3 GeV/c support this conclusion.⁵ Since the charge-exchange process producing K^{*0} proceeds through pseudoscalar exchange and the η coupling to the nucleons is small, pion exchange should dominate this reaction. There has not yet been sufficient data on the charge-exchange reactions to test the detailed predictions of the absorption models, in particular the momentum-transfer dependence.

In this paper we present the results of an analysis of $K^*(890)^0$ production in reactions (1.1) and (1.2) in terms of the absorptive peripheral model. ρ and ω couplings predicted by relativistic $SU(6)$ are used to give the couplings to the nucleon.⁶

The $K^*(1400)$ was first reported in 1965, as a $\bar{K}^0\pi^-$ enhancement in the reaction $K^-p \rightarrow \bar{K}^0\pi^-p$ at a K^- momentum of 3.5 GeV/c.⁷ It has since been observed in K^+p and π^-p interactions,⁸ through the decay modes $K\pi$, $K^*(890)\pi$, $K\omega$, $K\rho$, and $K\eta$. Its isotopic spin is one half, and a spin-parity assignment of 2^+ is favored but not conclusively established. A 2^+ spin-parity assignment allows the $SU(3)$ classification in a 2^+ octet to-

gether with the f^0 and A_2 mesons. On this assumption Glashow and Socolow have calculated the expected decay branching ratios.⁹ The predictions agree with the data within the rather large errors. The observed mass value varies from 1390 to 1480 MeV with a width varying from 60 to 160 MeV.¹⁰

The $K^*(1400)$ is strongly produced and appears in the final states (1.1) and (1.2) when decaying through the $K\pi$ mode. The resonance is also observed in the three-body decay modes in final states (1.3) and (1.4). We have used the events of reactions (1.2) and (1.4) to measure the decay branching ratios.

II. EXPERIMENTAL DETAILS

A. Beam Transport System

The high-momentum separated beam at the ZGS, shown in Fig. 1, uses two stages of electrostatic separation.¹¹ Two sextupoles (SX2 and SX3) are used to correct the chromatic aberration in each stage; octupoles are used between each quadrupole doublet to correct edge focusing effects. Pole-face coils are used in each bending magnet to achieve a uniform field (0.005% over a 7-in. aperture). These corrections, plus the use of magnetic slits, enabled the beam to be operated with only 5% contamination of pions and muons when tuned for 5.5-GeV/c K^- mesons. An internal target of copper-aluminum alloy 0.025 in. high \times 0.250 in. wide \times 3.0 in. along the beam was bombarded by 12.5-GeV protons. The target was placed inside the main ZGS guide field such that the K mesons were produced at 0° . With a solid angle of about $30 \mu\text{sr}$, the yield was about 4 K^- in the bubble chamber per 10^{11} protons incident on the target.

A threshold Čerenkov counter inside Q11 measured the light-particle contamination in the beam. This contamination was checked by scanning the film for δ rays having momenta greater than the maximum that can be produced by K mesons. The results were in good agreement with the measurements using the Čerenkov counter.

B. Exposures and Analysis

The exposures for this experiment consisted of 90 000 pictures at 4.1 GeV/c and 400 000 pictures at 5.5 GeV/c

⁴ A. Verglas, S. Focardi, A. Minguzzi-Ranzi, L. Monari, and P. Serra, *Nuovo Cimento* **41**, 629 (1966).

⁵ S. Goldhaber, I. Butterworth, G. Goldhaber, A. A. Hirata, J. A. Kadyk, T. A. O'Halloran, B. C. Shen, and G. H. Trilling, in *Proceedings of the Twelfth Annual International Conference on High-Energy Physics, Dubna, 1964* (Atomizdat, Moscow, 1966), Vol. 1, p. 711.

⁶ B. Sakita and K. C. Wali, *Phys. Rev.* **139**, B1355 (1965).

⁷ N. Haque, D. Scotter, B. Musgrave, W. M. Blair, A. L. Grant, I. S. Hughes, P. J. Negus, R. H. Turnbull, A. A. Z. Ahmad, S. Baker, L. Celnikier, S. Misbahuddin, H. J. Sherman, I. O. Skillicorn, A. R. Atherton, G. B. Chadwick, W. T. Davies, J. H. Field, P. M. D. Gray, D. E. Lawrence, J. G. Loken, L. Lyons, J. H. Mulvey, A. Oxley, C. A. Wilkinson, C. M. Fisher, E. Pickup, L. K. Rangan, J. M. Scarr, and A. M. Segar, *Phys. Letters* **14**, 338 (1965).

⁸ L. M. Hardy, S. U. Chung, O. I. Dahl, R. I. Hess, J. Kirz, and D. H. Miller, *Phys. Rev. Letters* **14**, 401 (1965); S. Focardi, A. Minguzzi-Ranzi, P. Serra, L. Monari, S. Herrier, and A. Verglas, *Phys. Letters* **16**, 351 (1965); J. Badier, M. Demoulin, J. Goldberg, B. P. Gregory, C. Pelletier, A. Rouge, M. Ville, R. Barloutaud, A. Leveque, C. Louedec, J. Meyer, P. Schlein, A. Verglas, D. J. Holthuizen, W. Hoogland, J. C. Kluyver, and A. G. Tenner, *ibid.* **19**, 612 (1965).

⁹ S. L. Glashow and R. H. Socolow, *Phys. Rev. Letters* **15**, 329 (1965).

¹⁰ A. H. Rosenfeld, A. Barbaro-Galtieri, W. J. Podolsky, L. R. Price, P. Soding, C. G. Wohl, M. Roos, and W. J. Willis, *Rev. Mod. Phys.* **39**, 1 (1967).

¹¹ T. H. Fields, E. L. Goldwasser, and U. E. Kruse, Argonne National Laboratory Report THF/ELG/UEK-1, 1961 (unpublished); R. Ammar, T. H. Fields, M. Derrick, E. L. Goldwasser, M. L. Good, U. E. Kruse, D. Reeder, F. Schweingruber, J. D. Simpson, in *Proceedings of 1966 International Conference on Instrumentation for High-Energy Physics, Stanford USAEC Conference 660918*, p. 620 (unpublished).

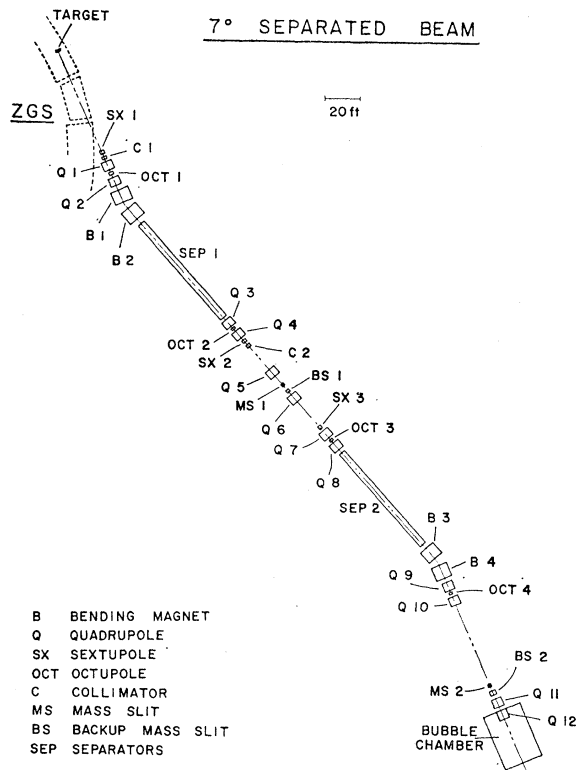


FIG. 1. Layout of high-momentum separated beam at the ZGS. The target can be placed to give any production angle, for negative particles, from 0° to the channel angle of 7.75° . Quadrupoles Q1 and Q2 make the beam parallel in the vertical plane and converge to a focus at C2 in the horizontal plane. Quadrupoles Q3 and Q4 make a vertical focus at the first mass slit MS1 and in the horizontal plane image the momentum source point (between B1 and B2) to MS1. Except for slight differences in magnet spacing and the absence of a second momentum collimator, the second stage is a mirror image of the first stage. This allows a vertical and a horizontal focus at the final mass slit and also a momentum coalescence. That is, the off-momentum rays not only focus at the same point, they have the same angles. Two sextupoles (SX 2 and SX 3) are used to correct chromatic aberration in each stage, and octupoles are used between each quadrupole doublet to correct edge focusing effects. Pole-face coils are used in each bending magnet to achieve a uniform field (0.005% over a 7 in. aperture). These corrections plus the use of magnetic slits enabled the beam to be operated with only 5% contamination of pions and muons when tuned for 5.5 GeV/c K^- mesons. The momentum bite, defined by collimator C2, was set at $\pm 1\%$. With this momentum spread, the effect of the sextupoles was to sharpen the image at the final mass slit to about 0.035 in., which was one-half the uncorrected height for the extreme rays. The mass slits were each set with a gap of 0.040 in. With the 50 ft of separator in each stage operated at 380 kV across the 2.25-in. gap, the π - K separation at 5.5 GeV/c was 0.055 in. The beam length from target to bubble chamber is about 350 ft.

in the 30-in. hydrogen bubble chamber.¹² The beam momentum for each exposure was measured by using τ decays fitted with the magnitude of the beam mo-

¹² The bubble chamber is a cylinder 30 in. in diameter and 15-in. deep, giving a useful volume of 200l. Two glass windows allow dark-field illumination of the four views recorded on 70-mm film. The magnetic field of 32.5 kG is provided by a conventional magnet using 5 MW of electrical power. Three pistons above the visible volume are used to provide the expansion. J. W. Mark, R. E. Picha, L. Voyvodic, A. Peekna, and W. D. Walker, in Proceedings

mentum treated as an "unmeasured" quantity. The actual momentum distributions so determined were centered at 4.07 and 5.47 GeV/c with full widths of 0.08 GeV/c.

All the film was double scanned for two-prong-plus- V events with a combined scan efficiency of $>99\%$. This yielded 4000 events at 4.1 GeV/c and 17 000 events at 5.5 GeV/c which were used in the analysis presented here. A separate scan for two-prong events was made on 34 700 frames at 4.1 GeV/c and 60 700 frames at 5.5 GeV/c. A slow, critical second scan was then made on 10% of this film to determine the scan efficiency and study scan biases for an analysis of elastic scattering.¹³ All two-prong events found in the first scan were processed and are used in the distributions reported here. The first scan efficiency for two-prong events was about 90%.

All of the scanned events were measured¹⁴ and processed by the reconstruction and kinematic fitting programs. After study of the spatial distribution of events, a rectangular fiducial volume was defined and was used in the post-kinematic programs for calculating cross sections, determining the effect of escape corrections, and investigating the possibility of biases in the distributions.

The total length of K^- beam track considered for each topology at each momentum was calculated from the number of τ decays represented by three-prong events observed in the scan volume. Other factors used when calculating cross sections were: escape corrections, scan efficiencies, misidentified events, χ^2 probability cutoffs, and losses due to failures in the reconstruction program. Reconstruction failures occurred for about 12% of the two-prong-plus- V events and about 7% of the two-prong events. All of the two-prong-plus- V failures were remeasured and are included in the results presented in this paper. These events were found to have the same distribution among the kinematic fit hypotheses, within statistics, as those events which passed after one measurement.

For interactions of the two-prong-plus- V topology, corrections must be made to cross sections and various angular distributions to account for lost events in which the V was not seen because of the limited chamber size or because the decay length was too short. This was

of 1966 International Conference on Instrumentation for High-Energy Physics, Stanford USAEC Conference 660918, p. 106 (unpublished).

¹³ J. Mott, Ph.D. thesis, Northwestern University, 1967 (unpublished).

¹⁴ All the events found in scanning were measured on conventional, measuring machines in which a cross hair was visually superimposed on a track image. The least count of the digitizers which recorded the X - Y coordinates on film was 1.5μ , but measurements were typically made to an accuracy of about 5μ . Between 5 and 10 points were measured on each track of a typical event using three of the four views available. K. Derrick, in *Proceedings of Twelfth Annual International Conference on High-Energy Physics, Dubna, 1964* (Azomizdat, Moscow, 1966), Vol. 2, p. 395; D. Gold, P. Yerkes, F. Schweingruber, IEEE Trans. Nucl. Sci. 13, 2 (1966).

done by assigning an appropriate weight to each event.¹⁵ The total weighting calculated for all K^0 events was in good agreement with the number of lost events as determined from a study of the distribution of times of flight of the K^0 's.

For peripheral interactions in which K^* 's are produced, the escape corrections are larger than for all other \bar{K}^0 final states. For $K^*(890)^-$ quasi-two-body production the average weightings were found to be 1.20 at 4.1 GeV/c and 1.27 at 5.5 GeV/c. The angular distributions presented in this paper were studied both with and without escape corrections and it was found that the escape corrections had a negligible effect on the results. The effect of the escape corrections on the production angular distribution of the $K^*(890)$ is shown by the shaded area of Fig. 12. The remaining distributions are less sensitive to this correction and the effects of the escape corrections are not shown.

The series of major computer programs used for organization, reconstruction, kinematic fitting, summarizing, and plotting results for this experiment consisted of MASMER-HGEOM-GRIND-SUMTAP-SUMEDIT-SUMX.¹⁶ Initial scan information for each event, including bubble-density estimates, mass guesses, and miscellaneous track information, was punched onto a single IBM card. These cards were used to make paper tapes for input to the computers on line to the measuring tables at ANL,¹⁴ and were also used as input to program MASMER to make the initial master list of events.

C. Precision and Program Reliability

The photographs for this experiment consisted of four views of the chamber for each exposure on a single strip of 70-mm film. The system of optics necessary to accomplish this¹⁷ made it difficult to directly determine the effective positions of the camera axes by survey methods. For reconstruction purposes the camera positions were determined by using a program (CAMAJUST), which fitted film measurements of fiducials and solved for optical parameters one camera at a time. This program was also used to measure the accuracy of recon-

struction using known fiducial positions on the chamber windows.

From the CAMAJUST studies it was determined that the standard deviation on the location of corresponding points in space was less than 0.01 cm. in the plane perpendicular to the magnetic field (x - y plane) and 0.05 cm. in the z direction. From track reconstruction, the rms scatter of measured track points from the fitted curve in the x - y plane was about $8\ \mu$ on film (0.01 cm. in space) for the first exposures and $11\ \mu$ for the later film. This difference can probably be attributed to the two γ -conversion plates used in the first exposures. Their absence in the later exposures permitted a larger fiducial volume, with tracks about 50% longer, leading to larger multiple scattering error and thus larger deviations in fitting the calculated space trajectories.

The general reliability of track swimming and error assignments was examined by looking at the distributions of "stretches" on the track parameters from kinematical fitting. These distributions were found to be properly centered about zero and to have nearly the widths expected. The χ^2 probability distributions were examined for both 4-constraint and 1-constraint fits and in all cases were found to be approximately uniform.¹⁸

The high magnetic field (32 kG) in the 30-in. bubble chamber and the high optical precision permit accurate

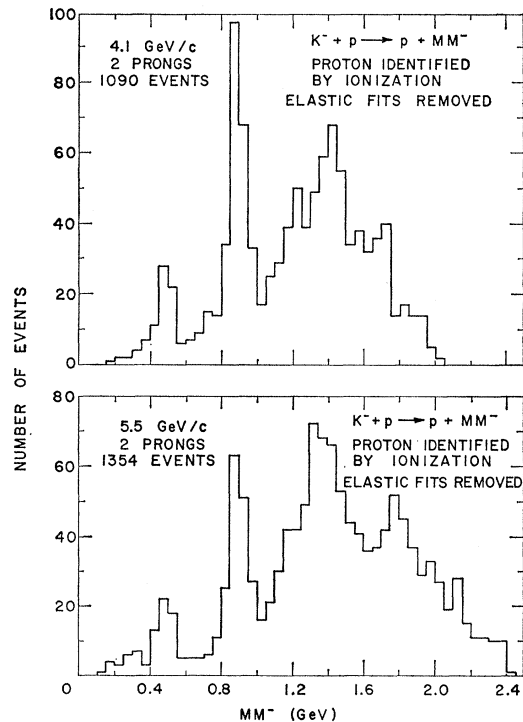


FIG. 2. Missing mass from proton for two-prong events in which the positive track was identified as a proton by bubble density as shown in Fig. 3. Events filling the elastic-scattering hypothesis have been removed. In addition to the well-known resonances at 0.89 and 1.4 GeV, there is a significant peak at about 1.8 GeV in the 5.5-GeV/c data.

¹⁵ For further details see F. Schweingruber, Ph.D. thesis, Northwestern University, 1967 (unpublished).

¹⁶ Geometrical reconstruction and kinematical fitting were accomplished by HGEOM and GRIND, respectively. HGEOM is a revised version of the three-view geometry program written at Rutherford Laboratory, England. Major revisions at ANL included facilities for using any two or three of four views, reading and writing master-list tapes in a new format, and handling of stopping tracks, mass assignments, and standard errors in a different manner. GRIND has been revised from the CERN version to handle new master-list formats and to properly treat track parameters and uncertainties as supplied by HGEOM. The final output master-list from GRIND contained all the information available for each event, including initial scan information, measurement data, reconstruction results, and results of kinematical fitting to each possible hypothesis. Descriptive writeups of each of the programs discussed in this paper can be obtained from the High-Energy Physics Program Library, Argonne National Laboratory, Argonne, Illinois.

¹⁷ J. A. Froehlich, Report No. JAF-1, Argonne National Laboratory, 1965 (unpublished).

measurements of the quantities used in kinematic testing and fitting. Additional checks were provided on the over-all reliability of the programs, optical constants, magnetic field, and chamber conditions by checking masses and widths of known resonances and particles. Examples of these checks are as follows.

(1) Gaussian resolution functions were plotted for the $K\pi$ invariant mass in the $K^*(890)^{0,-}$ and $K^*(1400)^{0,-}$ regions. The full widths of these functions were about 0.020 and 0.056 GeV for $K^*(890)^0$ and $K^*(1400)^0$, respectively, from the two-prong events; and 0.012 and 0.018 GeV for $K^*(890)^-$ and $K^*(1400)^-$, respectively, from the two-prong-plus- V events. The measured mass and width of the $K^*(890)^{0,-}$ given in Table IV are in good agreement with the known values.

(2) The missing-mass (MM) plots of Fig. 2 show that about 98% of the true elastic scattering events successfully fit this hypothesis. Before removing the elastic events from these plots, a fit was made to the K^- missing-mass peak and the mass was observed to be 0.494 ± 0.001 GeV at 4.1 GeV/ c and 0.493 ± 0.001 GeV at 5.5 GeV/ c , in good agreement with the known value of 0.4938 ± 0.0001 .

D. Analysis of Two-Prong Events

The hypotheses used in kinematic fitting of the two-prong events were the following:

$$K^-p \rightarrow K^-p \quad (2.1)$$

$$\rightarrow K^-p\pi^0 \quad (2.2)$$

$$\rightarrow K^-p\eta \quad (2.3)$$

$$\rightarrow \pi^-pK^0 \quad (2.4)$$

$$\rightarrow \pi^-p\pi^+\Delta \quad (2.5)$$

$$\rightarrow \pi^-p\pi^+\Sigma^0 \quad (2.6)$$

$$\rightarrow K^-p\pi^+n. \quad (2.7)$$

Other reactions which are likely but which are not kinematically overdetermined are as follows:

$$K^-p \rightarrow K^-p + MM \quad (B=0, S=0) \quad (2.8)$$

$$\rightarrow \pi^-p + MM \quad (B=0, S=-1) \quad (2.9)$$

$$\rightarrow \pi^-p\pi^+ + MM \quad (B=1, S=-1) \quad (2.10)$$

$$\rightarrow K^-p\pi^+ + MM \quad (B=1, S=0). \quad (2.11)$$

Hypotheses with two or more strange particles in the final state were not considered. These contribute less than 5% to the total number of two-prong events observed, as determined from a study of the multi-strange-particle events of more complicated topology.

Events which fit elastic scattering, hypothesis (2.1), were classified as such regardless of how well they fit other hypotheses, and were removed from the sample

considered for inelastic processes.¹⁸ Of the remaining events only 35% at 4.1 GeV/ c and 25% at 5.5 GeV/ c could be uniquely assigned to a single hypothesis using the kinematic variables and bubble-density information. This situation made it impossible to identify reactions on an event-by-event basis. However, events in certain kinematical configurations were much less ambiguous, and properties of this subsample could be studied with more confidence. Also, information obtained from the two-prong-plus- V events has been used to estimate the magnitude of the effect of misidentified events in various distributions.

For those events with momentum of the positive track less than about 0.750 GeV/ c , the bubble density could be used to distinguish between a proton and a π^+ . Bubble-density estimates made by the scanners were thus used to obtain a clean sample of events in which the positive track was identified as a proton. Figure 2 shows the distribution of the missing mass for the system of negative charge produced with the proton. The elastic scattering events have been removed. Since the protons identified in this way were necessarily of low momentum this selection was equivalent to making a momentum-transfer cut of a gradual nature, as determined by the scanners' mass-assignment efficiency. This efficiency was measured by looking at the assignments for elastic events (Fig. 3). The selection is approximately the same as a cut at $|t| < 0.5$ (GeV/ c)².

The K^* resonances are quite prominent in the mass plots of Fig. 2. The small peak at about 0.5 GeV is caused by the few elastic events which did not fit the elastic hypothesis. The sharp peak just below 0.9 GeV

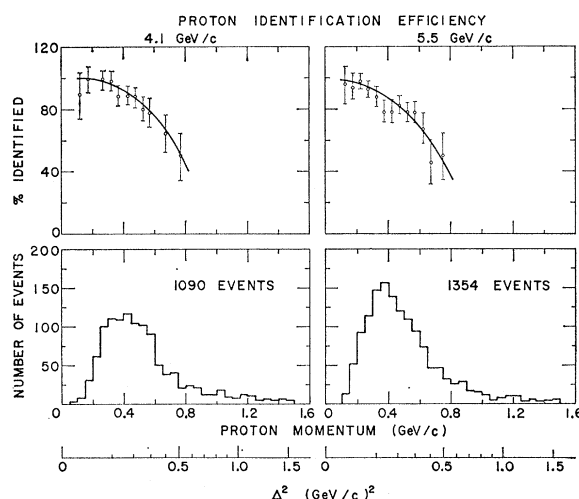


FIG. 3. The efficiency of the scanners for identifying protons using bubble density, plotted as a function of proton momentum. This efficiency was measured using events fitting to K^-p elastic scattering. Also shown is the distribution of proton momenta for the events whose missing mass is shown in Fig. 2.

¹⁸ J. Mott, R. Ammar, R. Davis, W. Kropac, A. Cooper, M. Derrick, T. Fields, L. Hyman, J. Loken, F. Schweingruber, and J. Simpson, Phys. Letters 23, 171 (1966).

is the well-known $K^*(890)$ resonance; these events should nearly all appear in the $K^-p\pi^0$ or $\bar{K}^0p\pi^-$ fitted events. The peaking around 1.4 GeV may represent in addition to the two-body and three-body decay of the $K^*(1400)$, any other $K\pi\pi$ enhancement in this mass range, including any resonances which would decay into a negative particle and two or more neutral particles.

At a beam momentum of 5.5 GeV/c there seems to be evidence for a K^* resonance in the region of 1.8 GeV,¹⁹ while at 4.1 GeV/c there is no significant peak although a slight enhancement may be observed at 1.7 GeV. The interpretation of these plots in the high-mass regions is made difficult by the lack of knowledge of the background distribution to be expected. No additional evidence for the enhancement at 1.8 GeV was found in the fitted two-prong events.

The $K^-\pi^+n$ final state is of particular interest because of neutral K^* resonances, and was therefore studied carefully. Although only about 15% of the fits to hypothesis (2.7) were unique based on the measurements of kinematic variables and bubble-density information, further analysis showed that most fits were indeed $K^-\pi^+n$ and certain cuts could be made to purify the sample.

Most of the ambiguities occurred between fits to hypothesis (2.7) ($K^-\pi^+n$) and hypotheses (2.5) and (2.6) ($\pi^+\pi^-\Lambda$ and $\pi^+\pi^-\Sigma^0$). Since each of these reactions contains a missing neutral hyperon their behavior can be studied in the two-prong-plus- V topology. In fact, the contributions to the two-prong events from all reactions with missing strange particles can be well determined from the two-prong-plus- V events using the known K^0 and Λ decay branching ratios and the calculated escape corrections. This method was used to investigate the ambiguous fits to the final state $K^-\pi^+n$.

Figures 4(a) and 4(b) show the missing mass from K^- and π^+ for all two-prong events, excluding only elastic scatters and events with a proton identified by ionization. The shaded events are those which fit the $K^-\pi^+n$ hypothesis with the restriction that the missing mass be in the range 0.70 to 1.18 GeV, and the fitted beam momentum be between 4.0 and 4.2 GeV/c for (a), and between 5.4 GeV/c and 5.6 GeV/c for (b). These cuts were chosen to purify the sample without giving rise to biases. The solid curves shown in Fig. 4 are the expected contribution from events with missing strange particles as determined by treating the two-prong-plus- V events as two prongs, calculating the missing mass as described above, and then giving a weight to each event based on

¹⁹ J. Bartsch, M. Deutschmann, E. Keppel, G. Kraus, R. Speth, C. Grote, J. Klugow, D. Pose, H. Schiller, H. Vogt, M. Bardadin-Otwinowska, V. T. Cocconi, P. F. Dalpiaz, E. Flaminio, J. D. Hansen, H. Hromadnik, G. Kellner, D. R. O. Morrison, S. Nowak, N. C. Barford, D. P. Dallman, S. J. Goldsack, M. E. Mermikides, N. C. Mukherjee, A. Frohlich, G. Otter, I. Wacek, and H. Wahl, Phys. Letters **22**, 357 (1966).

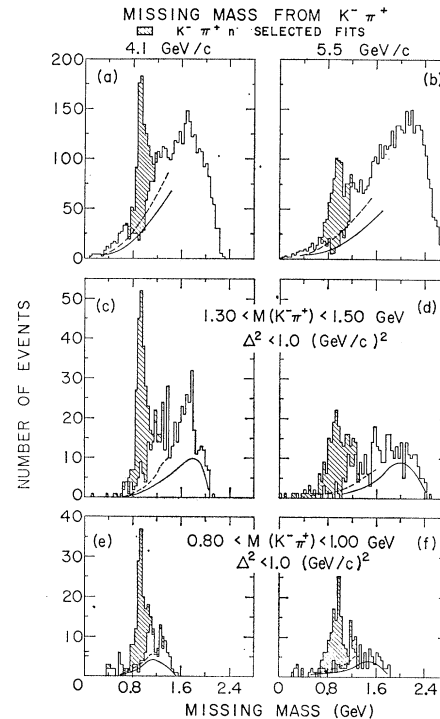


FIG. 4. Missing mass from K^- and π^+ for all two-prong events except those having a proton identified by ionization or fitting to the elastic scattering hypothesis. (a) and (b) represent all events, (c), (d), (e), and (f) have selections made on the $K^-\pi^+$ invariant mass and four-momentum transfer to obtain representative samples of the $K^*(890)^0$ and $K^*(1400)^0$ resonances. These selections are as follows: for (c) and (d) $1.30 \text{ GeV} < M(K^-\pi^+) < 1.50 \text{ GeV}$ and for (e) and (f) $0.80 \text{ GeV} < M(K^-\pi^+) < 1.00 \text{ GeV}$. For all four figures the four-momentum-transfer selection used was $\Delta^2(n) < 1.0 (\text{GeV}/c)^2$. The shaded events are fits to the hypothesis $K^-\pi^+n$ with the following restrictions: (1) Fitted beam momentum must be between 4.0 and 4.2 GeV/c for 4.1 GeV/c events and between 5.4 and 5.6 GeV/c for 5.5 GeV/c events. (2) Missing mass from $K^-\pi^+$ must be between 0.70 and 1.18 GeV for (a) and (b), and must be less than 1.35 GeV for (c), (d), (e), and (f). The lines show the estimated background from other reactions.

the identity of the neutral particle and the relative cross-section bases for the two topologies.

Another possible contribution to the background is the final state $K^-p\pi^0(\pi^0)$. The shape of this background was estimated by studying the final state $\bar{K}^0p\pi^-(\pi^0)$ in the two-prong-plus- V topology and assuming the distributions are independent of charge. Thus, the K^0 track was assigned a K mass, the proton track was assigned a π mass, and the missing mass from these two tracks was plotted. The dotted curves of Fig. 4 show the shape of this distribution when added to the previous background. The normalization of this additional background was estimated only roughly. Events of the final state $K^-\pi^+n\pi^0$ might also fit to the $K^-\pi^+n$ hypothesis, and some evidence for this is seen in the plots of Fig. 4, although this ambiguity is obviously not serious.

Figures 4(c), 4(d), 4(e), and 4(f) show the missing-mass distributions when additional selections are made on the $K^-\pi^+$ invariant mass and on the momentum transfer

to the $K^-\pi^+$ system in order to select clean samples of the $K^*(890)$ and $K^*(1400)$ resonances.

A further check on the purity of the sample was made by looking at the " $K^-\pi^+$ " mass distribution for the two types of background represented by the curves on Fig. 4 when the "missing mass" was in the region of the neutron. The distributions were flat within statistics and had no anomalous mass peaks which would interfere with study of the resonances. The misidentified events were therefore subtracted from the resonance signal by the same techniques used to subtract nonresonant background. In fact, this procedure should be more successful for misidentified-event background since this effect is necessarily noninterfering.

E. Analysis of Two-Prong-Plus- V Events

The kinematic fitting of two-prong-plus- V events was done by GRIND in three steps.

(1) The V was tried as a Λ , $\bar{\Lambda}$, and K^0 . This resulted in a unique fit for 81% of the V 's at both 4.1 and 5.5 GeV/ c .

(2) Using the results from the V fit for the neutral decaying track, a fit was attempted at the primary vertex for a large number of hypotheses. If more than one V fit was successful in step 1, hypotheses for the primary vertex included those for each successful fit for the decaying neutral.

(3) Using each of the fits from step 2, a multivertex fit was made which incorporated both steps 1 and 2 simultaneously for the appropriate hypotheses. This multivertex fit was attempted only if the measured beam momentum was within two standard deviations of the accepted beam momentum for that run. The analysis of events was made using these multivertex fits.

The two-prong-plus- V hypotheses used in GRIND of concern to this experiment were:

$$K^-p \rightarrow \bar{K}^0\pi^-p \quad (2.12)$$

$$\rightarrow \bar{K}^0\pi^-\pi^0p \quad (2.13)$$

$$\rightarrow \bar{K}^0\pi^+\pi^-n. \quad (2.14)$$

For the events with the V identified as a K^0 there are also a large number of 1-constraint hypotheses in which there is more than one strange particle in the final state. These were tried in GRIND, but since the results of an analysis of the multi-strange-particle events indicate that such events should contribute less than 5% to all of the two-prong-plus- V events fits to these hypotheses were rejected if there was a satisfactory fit to one of the above hypotheses.

Hypothesis (2.12) is a four-constraint production fit with no unseen particles. Of the fits to this reaction 98% were unique at 4.1 GeV/ c and 94% were unique at 5.5 GeV/ c . No attempts were made to purify the sample further. The purity is almost certainly better than these

percentages suggest since most of the ambiguities were with 1-constraint fits.

Reaction (2.13) is not studied extensively in this paper because of the very complicated structure in the $\bar{K}^0\pi^-\pi^0$ invariant mass which peaks strongly in the mass region of 1.2 to 1.5 GeV. This peaking makes it difficult to determine the contribution of the $K^*(1400)$ to this final state. The structure is probably connected with production of $K\pi\pi$ resonant states via a diffraction mechanism which does not operate in reaction (2.14). For the plots presented in Sec. V, all fits with a χ^2 probability greater than 5%, which satisfied bubble-density criteria, and for which the missing mass was less than $2m_\pi$, were used. With these criteria and using a 5-times χ^2 probability ratio cutoff, 95% of the events at 4.1 GeV/ c provided unique fits and 72% were unique fits at 5.5 GeV/ c . The final state $\bar{K}^0\pi^+\pi^-n$, reaction (2.14), was used for studying the 3-body decay of the $K^*(1400)$. In this final state the $K\pi\pi$ invariant mass distribution is not dominated by the large peak at low masses which is predominant in reaction (2.13), and in the region of 1.4 GeV the $K\pi\pi$ mass distribution more closely follows the expected behavior for phase space plus a resonance.

To investigate the reliability of fits to hypothesis (2.14) we have plotted the missing mass from $\pi^-\pi^+$ and K^0 for all two-prong-plus- V events in which the V is identified as a K^0 . An additional requirement that the $K\pi\pi$ invariant mass be between 1.10 and 1.70 GeV was used in Fig. 5 to obtain a sample which shows the problems of misidentified events in the $K^*(1400)$ region. The shaded events are the distribution of fits to $\bar{K}^0\pi^+\pi^-n$ as determined from a selection with a χ^2 probability greater than 5% with an estimated normalization. The background in the missing-mass plots of Fig. 5 comes primarily from the final states $\bar{K}^0\pi^-p + MM^0$. The properties of these final states have not been studied extensively, but the background is sufficiently low that the effects of misidentified events should be removed by the normal background subtraction techniques.

The plots of Fig. 5 show some evidence for the final state $\bar{K}^0\pi^-\pi^+N^*(1236)^0$, and the discrimination between missing neutron and missing N^* is quite good. At 4.1 GeV/ c no events with N^* missing appear to be incorrectly identified as reaction (2.14), while at 5.5 GeV/ c the contamination from this is only a few percent.

III. RESULTS ON $K\pi N$ FINAL STATES

A. $K\pi N$ Phase-Space Distributions

The distribution of three-body final states $K^-\pi^+n$ and $\bar{K}^0\pi^-p$ are presented in the form of Dalitz plots in Figs. 6 and 7. The $K^-\pi^+n$ events plotted in Fig. 6 are those shaded in Figs. 4(a) and 4(b) with the additional restriction that the χ^2 probability for the fit must be better than 5% and the vertex of the event must be in a fiducial volume chosen such that the length of each

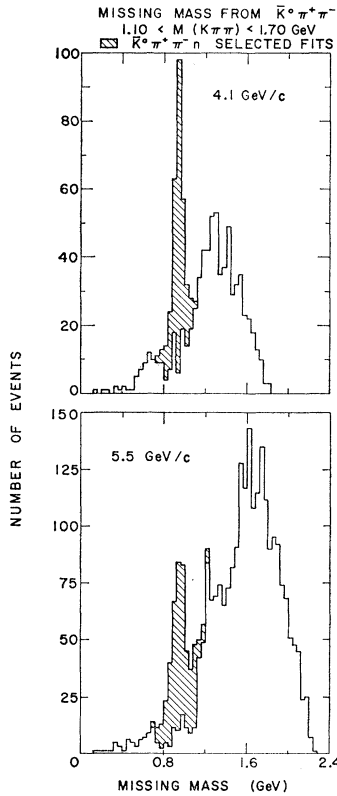


FIG. 5. Missing mass for the $K^*(1400)^0$ events. The missing mass from $\bar{K}^0\pi^+\pi^-$ system is shown for all two-prong-plus- V events in which the V was identified as a \bar{K}^0 and the positive prong was not identified as a proton (a) at 4.1 GeV/c and (b) at 5.5 GeV/c. The selection $1.10 \text{ GeV} < M(K\pi\pi) < 1.70 \text{ GeV}$ is made on the $K\pi\pi$ mass. The shaded region shows the distribution of missing mass for all events that fit the $\bar{K}^0\pi^+\pi^-$ hypothesis with a χ^2 probability greater than 5%. The normalization of the shaded events has been estimated.

secondary was at least 10 cm. Similar plots were also made for the $K^-\pi^+n$ fits from the two-prong-plus- V events analyzed as two prongs. These distributions appeared uniform within statistics over the Dalitz plot, so that misidentified events from missing strange-particle reactions should not cause appreciable errors in interpretation of the distributions of Fig. 6. The level of background from this source is about 14% at 4.1 GeV/c and about 20% at 5.5 GeV/c. The $\bar{K}^0\pi^-p$ events plotted in Fig. 7 include only those from the two-prong-plus- V topology. The only selection criterion was that the χ^2 probability for the fit must be greater than 1%.

The $K^*(890)$ band is prominent on each of the Dalitz plots of Figs. 6 and 7 and the $K^*(1400)$ is also quite evident. N^* and Y^* production appear to be small in the $\bar{K}^0\pi^-p$ final state, while in the $K^-\pi^+n$ final state there is an accumulation of events in the low π^+n mass regions which is suggestive of substantial N^* production. $N^*(1236)$ is the only πN resonance which can be clearly identified, but other possibilities include $N^*(1525)$ and $N^*(1688)$.

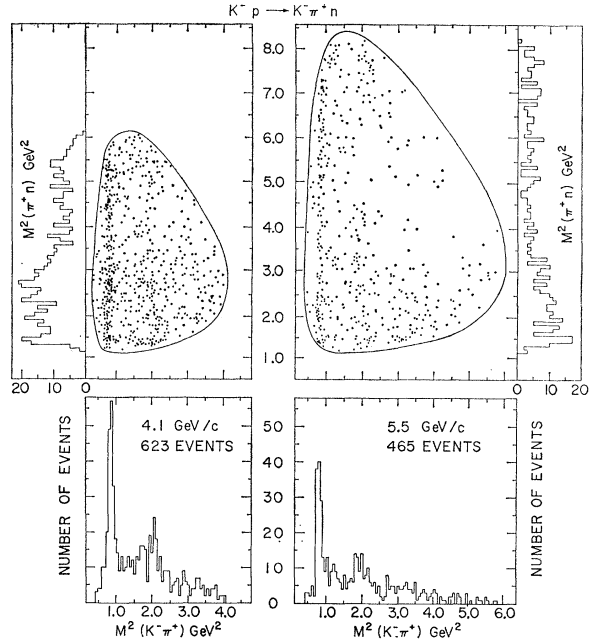


FIG. 6. Dalitz plots and projections for the final state $K^-\pi^+V$. The events plotted are those shaded in Figs. 4(a) and 4(b) with the additional restriction that the χ^2 probability for the fit must be better than 5% and the primary vertex must be in the selected fiducial volume. The $K^*(890)$ and $K^*(1400)$ bands are evident and $N^*(1236)$ production can be seen.

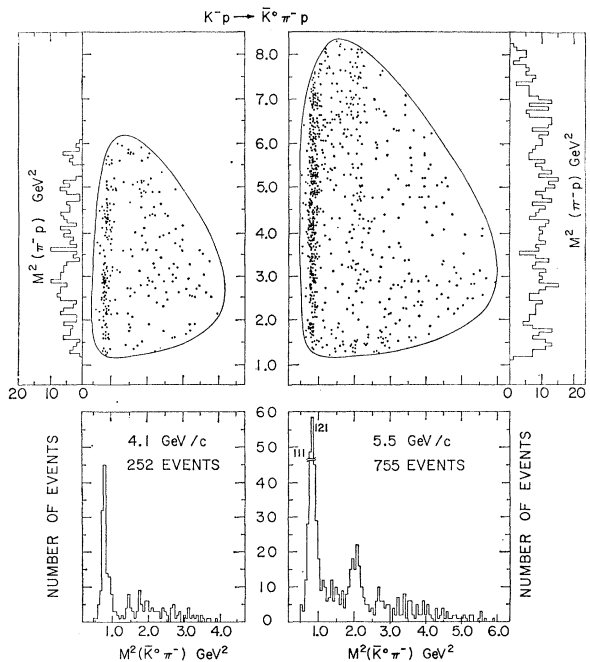


FIG. 7. Dalitz plots and projections for the final state $\bar{K}^0\pi^-p$. The plots show the 252 events at 4.1 GeV/c and 755 events at 5.5 GeV/c which fit to this final state in the two-prong-plus- V topology with χ^2 probabilities greater than 1%. The $K^*(890)$ and $K^*(1400)$ bands are the only clear examples of resonance production.

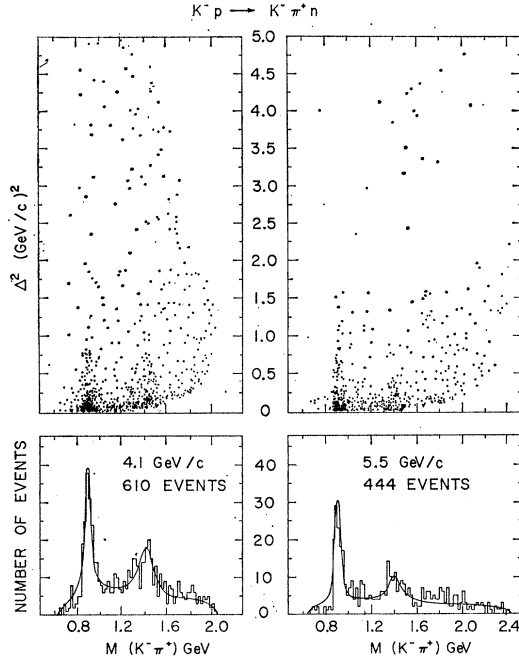


FIG. 8. Chew-Low plots and $K^-\pi^+$ mass projections for the final state $K^-\pi^+n$. Events plotted are the shaded events of Figs. 4(a) and (b) with χ^2 probability greater than 5% and with the primary vertex in a selected fiducial volume. The curve is the incoherent addition of phase space plus two Breit-Wigner functions fitted to the $K^-\pi^+$ mass distribution. The peripheral nature of the K^* production can be clearly seen with very few events produced at large momentum transfer.

Similar distributions were observed at 3.0 GeV/c in the $K^-\pi^+n$ final state⁴ but in that case most of the π^+n enhancement was associated with the $K^*(890)^0$ band. This led to an asymmetry in the $K^*(890)^0$ band across the Dalitz plot given by (upper half-lower half)/total = 0.21 ± 0.05 . In our data at 4.1 and 5.5 GeV/c we observe $K^*(890)^0$ asymmetries of 0.091 ± 0.07 and 0.084 ± 0.08 , respectively. These asymmetries are consistent with zero. We observed larger asymmetries when less restrictive cuts were used to select events.

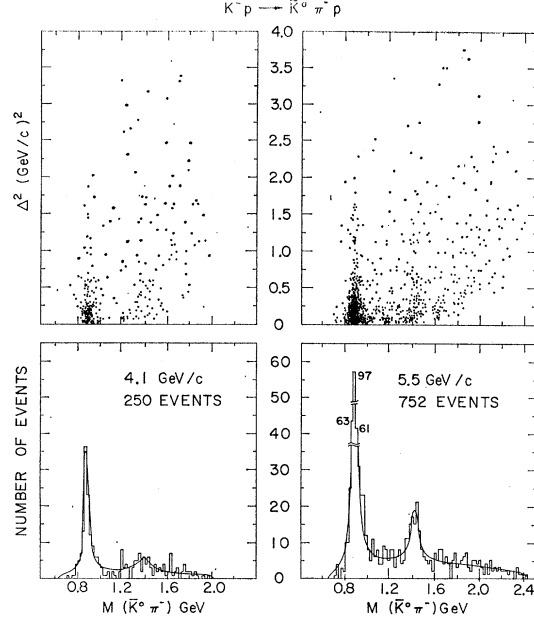


FIG. 9. Chew-Low plots and $\bar{K}^0\pi^-$ mass projections for the final state $\bar{K}^0\pi^-p$. Events plotted are all fits to this final state in the two-prong-plus- V topology with χ^2 probability greater than 1%. The curve is the incoherent addition of phase space plus two Breit-Wigner functions fitted to the $\bar{K}^0\pi^-$ mass distributions.

The peripheral nature of the K^* production process is illustrated in the Chew-Low plots of Figs. 8 and 9. $K^*(890)^{0,-}$ and $K^*(1400)^{0,-}$ are produced peripherally and no appreciable contribution above a very low background is seen in the backward direction for either charge state of each resonance at the two beam momenta. This is qualitatively in agreement with production by single-meson exchange. A backward peak would be expected for a baryon exchange process, but for these resonances, a baryon of strangeness $+1$ would be required, none of which are known to exist. The events observed in the backward direction are listed in Table I together with the upper limits on the cross sections. The

TABLE I. Backward production of $K^*(890)^{0,-}$ and $K^*(1400)^{0,-}$.

Reaction: $K^- + p \rightarrow$	Beam mom. (GeV/c)	Events in K^* bands		Normalized events from background bands		Cross-section limit (μb) (90% confidence)	
		$\theta > 90^\circ$	$\theta > 135^\circ$	$\theta > 90^\circ$	$\theta > 135^\circ$	$\theta > 90^\circ$	$\theta > 135^\circ$
$K^*(890)^{-} + p$	4.1	0	0	0	0	8.7	8.7
$\bar{K}^0\pi^-$	5.5	0	0	0	0	1.6	1.6
$K^*(890)^0 + n$	4.1	7	2	4	3	17.4	7.4
$K^-\pi^+$	5.5	2	2	4	3	6.4	6.4
$K^*(1400)^{-} + p$	4.1	1	0	4	0	8.7	8.7
$\bar{K}^0\pi^-$	5.5	1	0	1	0	1.6	1.6
$K^*(1400)^0 + n$	4.1	13	4	16	6	7.4	7.4
$K^-\pi^+$	5.5	6	4	10	4	6.4	6.4

limits obtained, of a few mb, are comparable to those for K^-p elastic scattering and about an order of magnitude less than for $\pi^\pm p$ elastic scattering in the same energy range.¹⁸

B. $K\pi N$ Production Cross Sections

From the Dalitz plots of Figs. 6 and 7 and the fits to phase space plus Breit-Wigner functions, shown on the projections of the Chew-Low plots of Figs. 8 and 9, we have determined the production cross sections for $K^*(890)^{0,-}$, $K^*(1400)^{0,-}$, and $N^*(1236)^{+,0}$ appearing in the final state $K\pi N$. Table II summarizes the results. The errors listed include the statistical error on the number of events and the uncertainty in the cross-section basis. For the reaction $K^-p \rightarrow K^-N^*(1236)^+$ an additional uncertainty exists because of the accumulation of events at low π^+n mass. The relative contributions to this region from N^* production, misidentified events, and nonresonant background are not completely understood and the possibility of interference between the crossing K^* and N^* bands adds further complications. Therefore, we list in Table II the number of events on the Dalitz plots that were estimated to be in each resonance, and were used for the cross-section determination. For the K^* resonances these estimates came from the fits to Breit-Wigner functions plus phase space.

Arnold²⁰ has proposed a Regge-pole model for charge-

TABLE II. $K\pi N$ production cross sections.

Reaction: $K^-+p \rightarrow$	No. of events on Dalitz plots—Figs. 6 and 7		Cross section (μb)	
	4.1 GeV/c	5.5 GeV/c	4.1 GeV/c	5.5 GeV/c
$\bar{K}^0\pi^-p$ total	252	755	730 ± 98	412 ± 41
$K^-\pi^+n$ total	546*	388*	1356 ± 162	832 ± 112
$K^*(890)^{-}+p$				
$\bar{K}^0\pi^-$	115	341	333 ± 41	186 ± 17
$K^*(890)^0+n$				
$K^-\pi^+$	149	118	370 ± 41	253 ± 32
$K^*(1400)^{-}+p$				
$\bar{K}^0\pi^-$	30	97	87 ± 19	53 ± 8
$K^*(1400)^0+n$				
$K^-\pi^+$	86	53	214 ± 33	114 ± 21
$N^*(1236)^0+\bar{K}^0$				
$p\pi^-$	4	27	12 ± 12	15 ± 5
$N^*(1236)^++K^-$				
$n\pi^+$	9	10	22 ± 20	21 ± 20

* Assuming misidentified events add 14% at 4.1 GeV/c and 20% at 5.5 GeV/c.

²⁰ R. C. Arnold, Phys. Rev. **153**, 1506 (1967). Preliminary results from this experiment for the N^* production cross sections at 5.5 GeV/c given in Fig. 4 of Arnold's paper are incorrect. The theoretical prediction for the cross section of the reaction $K^-p \rightarrow$

and hypercharge-exchange reactions which has been quite successful in explaining the energy dependence of the production cross sections for reactions of the type $PB \rightarrow PB^*$, where P is a pseudoscalar meson and B is a baryon. The cross sections for $N^*(1236)$ production in this type of reaction are expected to have the energy dependence

$$\sigma_t \propto E^2 k^{-4} s^{2(a_p)-1},$$

where: E = average of initial and final baryon energy in the c.m. frame,

k = average of initial and final momentum in the c.m. frame,

s = square of total c.m. energy,

$\langle a_p \rangle \cong 0.40$ is the average ρ_1-A_2 Regge trajectory over the region of maximum contribution in $d\sigma/dt$ versus t .

In this model the reactions

$$\pi^+p \rightarrow \pi^0\Delta^{++} \quad (3.1)$$

$$K^+p \rightarrow K^0\Delta^{++} \quad (3.2)$$

$$K^-p \rightarrow K^-\Delta^+ \quad (3.3)$$

$$K^-p \rightarrow K^0\Delta^0 \quad (3.4)$$

are related through $SU(3)$ Clebsch-Gordan coefficients and exchange degeneracy, so that the cross-section predictions for all of these reactions are established by a normalization to just one of the reactions at one energy. Figure 10 shows the predicted production cross section for these reactions normalized to the measured cross section for reaction (3.1) at 8 GeV/c, along with other data on these reactions. Also included are our results for reactions (3.3) and (3.4) at 4.1 and 5.5 GeV/c.²⁰ One sees that the theory fairly well predicts the observed behavior of the cross sections.

IV. PRODUCTION AND DECAY OF $K^*(890)^{0,-}$

A. $K^*(890)^{0,-}$ Production

$K^*(890)^{0,-}$ production is a prominent feature of the $K\pi N$ final states as can be seen on the scatter plots of Figs. 6 through 9 and the missing-mass plots of Fig. 2. The resonance is produced in each final state with about 15% nonresonant background in the $K\pi$ mass range from 0.830 to 0.960 GeV, which was the mass selection used for analysis.

For study of $K^*(890)^{-}$, the two-prong final states $K^-\pi^0p$ and $\bar{K}^0\pi^-p$ were used together with the $\bar{K}^0\pi^-p$ events from the two-prong-plus- V topology. The ambiguity problems for the two-prong events in the $K^*(890)^{-}$ mass band are much less severe than in the higher $K\pi$ mass regions. Of the events fitting $\bar{K}^0\pi^-p$ or $K^-\pi^0p$ in this band about 55% were unique on the basis of a

$\bar{K}^0\Delta^0$ is also incorrectly given in this reference. These errors are corrected in Fig. 10 of the present paper. We wish to thank D. D. Reeder for pointing out the discrepancies.

5-times χ^2 probability ratio requirement, and 20% were ambiguous only between these two hypotheses. The ambiguous events were then assigned according to the best fit, and the resulting distributions were in good agreement with requirements of isospin conservation in the decay of the $K^*(890)^-$.

For study of $K^*(890)^0$, all $K^-\pi^+n$ fits with a χ^2 probability greater than 5%, which satisfied bubble-density estimates, and with $K^-\pi^+$ invariant mass within the above mass-selection range were used. Misidentified events which could bias the analysis come primarily from events in which there is one or more missing

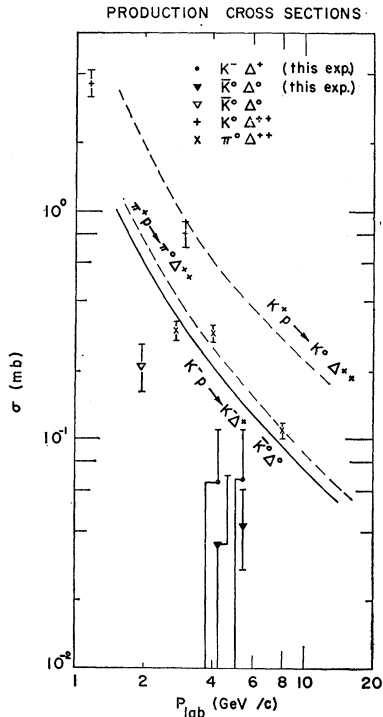


FIG. 10. Production cross sections for quasi-two-body production of $N^*(1236)$ and $K^\pm p$ and $\pi^\pm p$ interactions as a function of incident beam momentum including the data from this experiment. The curves are the predictions of the Regge-pole model of Arnold (Ref. 20), normalized to the reaction $\pi^+p \rightarrow \pi^0\Delta^{++}$ at 8 GeV/c.

neutral pions (e.g., $K^-p \rightarrow K^*0N^*0$). The missing-mass distributions for the accepted events were used to estimate this contamination which was about 7% at 4.1 GeV/c and 15% at 5.5 GeV/c.

When analyzing angular distributions, events from each side of the $K^{*0,-}$ peaks were used to investigate the effect of incoherent background and misidentified events. The mass selections used for this were 0.740 to 0.830 GeV and 0.960 to 1.040 GeV. The $K^*(890)$ distributions presented in this paper do not have this background subtracted since it was less than 20% and had negligible statistical effect.

Figures 11 and 12 show the production angular dis-

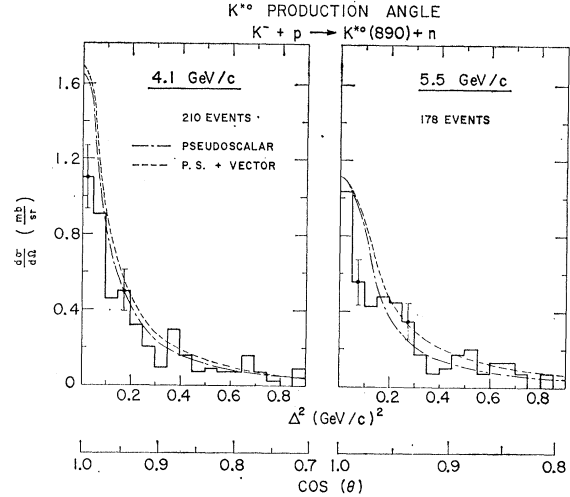


FIG. 11. $K^*(890)^0$ production angular distributions in the reaction $K^-p \rightarrow K^*(890)^0n$. The curves are the result of the absorptive-peripheral-model calculations described in Sec. IV B. No arbitrary normalization is used in comparing the curves with the data.

tributions for $K^*(890)^{0,-}$ at both energies. For $K^*(890)^-$ production in the two-prong events a scan bias against very peripheral events existed because of the short proton track. This was very similar to the case of elastic scattering, as discussed in detail by Mott.¹³ The bias was not present for the events in the two-prong-plus- V^0 topology since the V^0 provides a reliable signature and these events only were used to determine the population of the first bin in Fig. 12 at each energy.

There is a significant difference between the production angular distributions for the two different charge

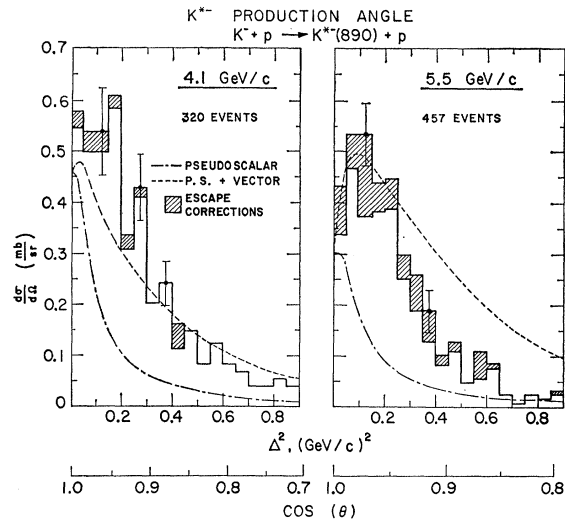


FIG. 12. $K^*(890)^-$ production angular distributions in the reaction $K^-p \rightarrow K^*(890)^-p$. The shaded regions show the contribution of the escape corrections. The curves are the result of the absorptive-peripheral-model calculations described in Sec. IV B. No arbitrary normalization is used in comparing the curves with the data.

states of the $K^*(890)$ resonance. The K^{*0} is seen to be peaked more sharply forward than K^{*-} , indicative of a lighter particle exchanged in the production process, and this behavior is also shown by the curves which include both the vector- and pseudoscalar-exchange contributions to $K^{*0,-}$ production. These curves are the distributions predicted by an exchange model with absorption as described in the next section.

B. Absorptive-Peripheral-Model Calculation

The absorptive-peripheral model was used to predict the production angular distributions as well as the density matrices. The method of calculation has been described in detail by Chilton *et al.*²¹ and is essentially different from the original method of Jackson in that an exact summation of partial waves is used instead of the impact-parameter approximation.

The starting point of the calculation is the so-called magic formula of Sopkovich²² which gives the expression for the partial-wave amplitude

$$M_{f_i^j} = (S_{f_i^j})^{1/2} B_{f_i^j} (S_{i_i^j})^{1/2}.$$

Here $B_{f_i^j}$ is the partial-wave Born amplitude and $S_{i_i^j}$ and $S_{f_i^j}$ are the elastic S -matrix elements for the initial and final states, respectively. The exponential decrease of the elastic scattering angular distribution and imaginary character of the forward scattering amplitude lead to a single expression for the elastic scattering S matrix. This is given by

$$S^i = \exp(2i\delta_j) = 1 - C \exp[-\gamma(j - \frac{1}{2})^2],$$

where

$$C = \sigma_t / 4\pi A, \quad \gamma = 1/2q^2 A,$$

and σ_t is the total scattering cross section for the initial (final) state particles. The parameter A specifies the elastic scattering exponential fall off in the form $d\sigma/dt \sim \exp(-At)$, and q is the center-of-mass momentum of the incident particles.

It is clear from the above discussion that only two parameters are needed to describe the effect of absorption in the initial states: σ_t and A . These have been measured in a previous experiment using this film.¹⁸ The effect of the final-state absorption is not so easy to determine; C and γ were estimated by using the copious data on the reactions $\pi^\pm p \rightarrow \rho^\pm p$ from 1.6 to 8.0 GeV/ c .³ No attempt was made to optimize the final-state absorption parameters. The values used were

$$\gamma_f = 0.75\gamma_i \quad \text{and} \quad C_f = 1.0.$$

In calculating the Born term, all pseudoscalar- and vector-exchange processes were taken into account. The coupling constants for a specific exchange mechanism were taken in the zero-momentum-transfer limit of relativistic $SU(6)$.⁶ There are basically three input

²¹ F. Chilton, D. Griffiths, and R. Jabbur, *Phys. Rev.* **153**, 1610 (1967).

²² N. J. Sopkovich, *Nuovo Cimento* **26**, 186 (1962).

parameters entering the calculations: the pion-nucleon coupling $g_{\pi^0 N N^2} = 15.0$; the ρ width was taken to be 120 MeV; and the experimental width of the K^* , used to give the $KK^*\pi$ coupling, was taken to be 50 MeV. It should be further noted that only Dirac (electric) type vector coupling is used, since the contribution of the Pauli (magnetic) coupling is negligible in the forward direction. At least 14 partial waves were used in each case, the criterion being to cut off when the absorption effect is less than 1%.

The $SU(6)$ couplings predict that the contribution to $K^*(890)^-$ production cross section from ω exchange should be nine times larger than the contribution from ρ exchange, and that in $K^*(890)^0$ production, where ω exchange cannot occur, the predominant mechanism should be π exchange. That these conditions are satisfied, within the accuracies of the absorption model and the data, is shown in Figs. 11 and 12. K^{*0} production (Fig. 11) fits well to pseudoscalar exchange alone or to pseudoscalar plus the small amount of vector (ρ) exchange predicted by $SU(6)$ which contributes about 15% to the cross section. Neglecting interference effects, the cross section for K^{*-} production by ρ exchange should be $\frac{1}{9}$ as much as K^{*0} production by ρ exchange. Thus the large vector-exchange contribution to K^{*-} production evident in Fig. 12 must be primarily ω exchange. It should be emphasized that the results of an absolute $SU(6)$ calculation are being compared with the data in Figs. 11 and 12. No arbitrary normalization was used.

C. $K^*(890)$ Decay Angular Correlations

The decay distributions of the $K^*(890)^{0,-}$ are determined by the spin-polarization distribution of the decaying resonance, and the polarization is determined, in turn, by the production process. Therefore, by analyzing the distribution of $K^*(890)$ decay products with respect to the incident beam direction and the production plane, one can obtain information about the spin of the resonance and about the exchange mechanisms by which the resonance is produced.

A convenient coordinate system for this analysis is defined as follows: In the rest frame of the resonance, choose \hat{z} in the direction of the incident beam particle and \hat{y} normal to the production plane: $\hat{y} = (\mathbf{P}_i \times \mathbf{N}_f) / |\mathbf{P}_i \times \mathbf{N}_f|$, where \mathbf{P}_i and \mathbf{N}_f are the momenta of the target proton and final-state nucleon in the rest frame of the resonance. The third axis is then defined by $\hat{x} = \hat{y} \times \hat{z}$.

For two-body decays of the resonance, the decay distribution is expressed in terms of the polar angle θ and the azimuthal ϕ of one of the decay products. Since the two decay products are antiparallel in the rest frame of the resonance this completely specifies the decay. For $K^*(890)^{0,-}$ decay, θ is the angle between the incoming K^- and outgoing π and ϕ is the azimuthal angle of the π about the z axis, in the K^* rest frame. The usual

TABLE III. $K^*(890)^{0,-}$ spin-density matrix elements.

Δ^2 cut (GeV/c) ²	ρ_{00}		$\rho_{1,-1}$		$\text{Re}\rho_{10}$	
	4.1 GeV/c	5.5 GeV/c	4.1 GeV/c	5.5 GeV/c	4.1 GeV/c	5.5 GeV/c
	$K^- + p \rightarrow K^*(890)^- + p$					
0.0-1.0	0.224±0.038	0.124±0.027	0.325±0.029	0.311±0.027	-0.031±0.019	-0.028±0.016
0.0-0.1	0.400±0.100	0.281±0.073	0.300±0.090	0.254±0.060	-0.066±0.038	-0.063±0.037
0.1-0.2	0.150±0.072	0.057±0.037	0.325±0.067	0.379±0.058	-0.032±0.036	-0.063±0.026
0.2-0.4	0.132±0.062	0.129±0.046	0.356±0.053	0.336±0.044	-0.034±0.036	0.007±0.027
0.4-1.0	0.226±0.086	0.100±0.070	0.329±0.067	0.369±0.074	0.012±0.040	-0.009±0.045
	$K^- + p \rightarrow K^*(890)^0 + n$					
0.0-1.0	0.500±0.054	0.522±0.060	0.044±0.042	0.147±0.041	-0.053±0.032	-0.030±0.026
0.0-0.1	0.550±0.082	0.760±0.088	-0.033±0.067	0.047±0.068	-0.070±0.051	-0.166±0.048
0.1-0.2	0.612±0.112	0.500±0.150	0.020±0.099	0.100±0.070	-0.185±0.059	-0.271±0.075
0.2-0.4	0.378±0.126	0.438±0.124	0.095±0.094	0.239±0.099	0.085±0.069	-0.096±0.057
0.4-1.0	0.360±0.116	0.260±0.110	0.179±0.087	0.211±0.089	-0.025±0.064	0.014±0.066

requirements restrict the density matrix for the $K^*(890)$ to the form²³

$$\rho = \begin{pmatrix} \frac{1}{2}(1-\rho_{00}) & \rho_{10} & \rho_{1,-1} \\ \rho_{10}^* & \rho_{00} & -\rho_{10}^* \\ \rho_{1,-1} & -\rho_{10} & \frac{1}{2}(1-\rho_{00}) \end{pmatrix},$$

where ρ_{00} and $\rho_{1,-1}$ are real and ρ_{10} is complex. The diagonal matrix elements have physical interpretation as probabilities and therefore $0 \leq \rho_{00} \leq 1$, and the requirement that all eigenvalues of the density matrix be real adds the constraints

$$\rho_{11} + \rho_{1,-1} > 0$$

and

$$\rho_{00}(\rho_{11} - \rho_{1,-1}) \geq \sqrt{2} |\rho_{10}|^2.$$

The decay angular distribution of a resonance can then be written in terms of these density-matrix

elements. For resonances with $J^P=1^-$ decaying by a parity-conserving interaction into two spinless bosons this distribution is

$$W(\theta, \phi) = (3/4\pi) [\rho_{00} \cos^2\theta + \frac{1}{2}(1-\rho_{00}) \sin^2\theta - \rho_{1,-1} \sin^2\theta \cos 2\phi - \sqrt{2} \text{Re}\rho_{10} \sin 2\theta \cos\phi].$$

Thus, by studying the decay angular distribution of the $K^*(890)$ one can determine three of the four independent parameters in the spin-density matrix.

The $K^*(890)^{0,-}$ decay angular distributions were fitted to the distribution $W(\theta, \phi)$ using a maximum-likelihood procedure, subject to the above constraints on the matrix elements. For this fitting the events were grouped into four different momentum-transfer regions to investigate the change in the spin-density matrix as a function of momentum transfer. Since single-particle exchange is a peripheral interaction only those events with $|t| < 1.0$ (GeV/c)² were considered. Table III gives the results of this fitting and Figs. 13 and 14 show these

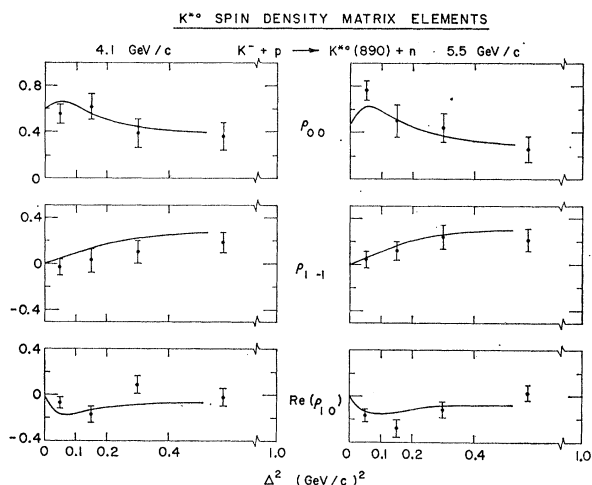


FIG. 13. Spin-density matrix elements as a function of four-momentum transfer for $K^*(890)^0$ produced in the reaction $K^-p \rightarrow K^*(890)^0n$. The Δ^2 bins used were: 0.0-0.1 (GeV/c)², 0.1-0.2 (GeV/c)², 0.2-0.4 (GeV/c)², and 0.4-1.0 (GeV/c)². The curves are the results of the absorptive-peripheral-model calculations and agree well with the data.

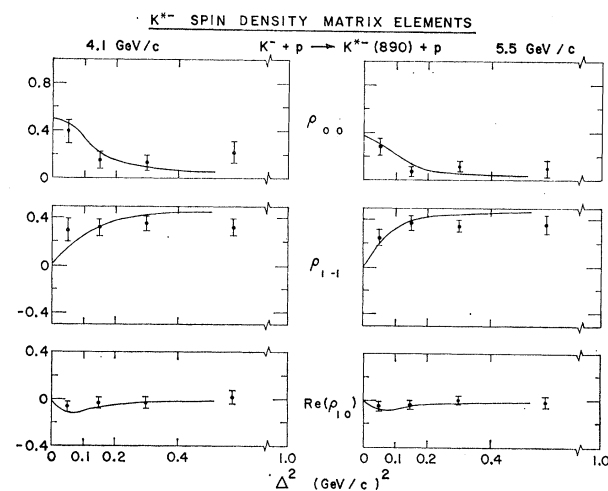


FIG. 14. Spin-density matrix elements as a function of four-momentum transfer for $K^*(890)^-$ produced in the reaction $K^-p \rightarrow K^*(890)^-p$. The Δ^2 bins used were as follows: 0.0-0.1 (GeV/c)², 0.1-0.2 (GeV/c)², 0.2-0.4 (GeV/c)², and 0.4-1.0 (GeV/c)². The curves are the results of the absorptive-peripheral-model calculations and agree well with the data.

²³ R. H. Dalitz, in *Proceedings of the International School of Physics, Enrico Fermi* (Academic Press Inc., New York, 1966), Course XXXIII, p. 141.

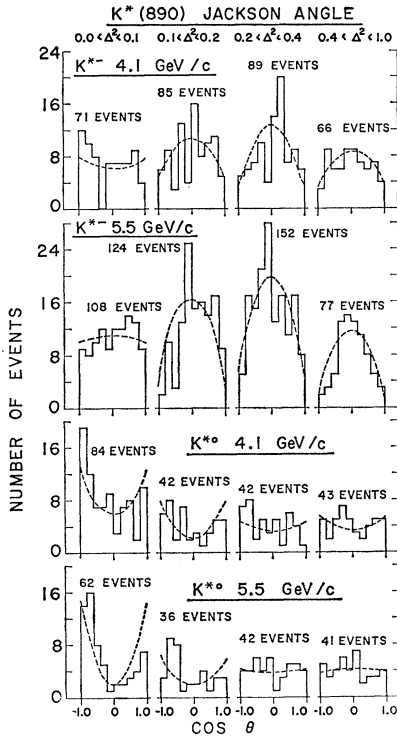


FIG. 15. Polar angle (Jackson angle, $\cos\theta$) distributions and best-fit curve for the events contributing to each data point on Figs. 13 and 14.

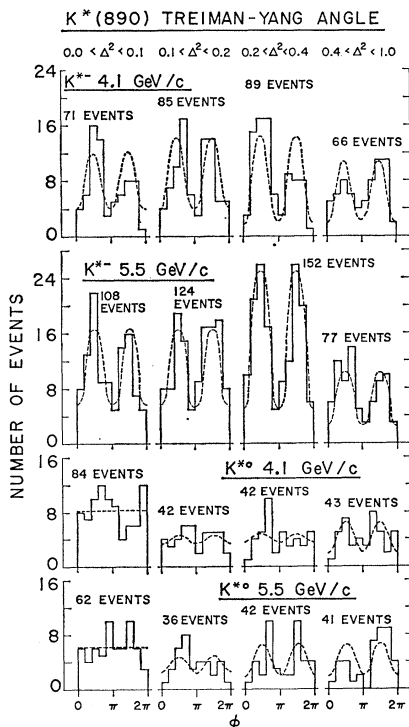


FIG. 16. Azimuthal angle (Treiman-Yang angle, ϕ) distributions and best-fit curve for the events contributing to each data point on Figs. 13 and 14.

results as well as the curves for pseudoscalar plus vector exchange predicted from the absorptive-peripheral-model calculation described in the previous section. The error bars on the experimental points extend to where the likelihood decreases by $1/e$.

When $W(\theta, \phi)$ is integrated over θ and ϕ separately, the expected distributions in each angle are

$$W(\theta) = (3/4\pi) [\rho_{00} \cos^2\theta + \frac{1}{2}(1 - \rho_{00}) \sin^2\theta],$$

$$W(\phi) = (1/4\pi^2)(1 - 2\rho_{1,-1} \cos 2\phi).$$

Figures 15 and 16 show the experimental data and expected distributions in θ and ϕ from the results of the maximum-likelihood fits given in Table III. The symmetries which are required by the expressions for $W(\theta)$ and $W(\phi)$ appear to be satisfied, within statistical uncertainties, except for the $\cos\theta$ distribution for the most peripheral region of $K^*(890)^0$ production. At both 4.1 and 5.5 GeV/c an asymmetry appears which is probably not a statistical fluctuation. The cause of this asymmetry has not been determined, but a possible source might be interference between K^* and N^* production.

The agreement displayed in Figs. 11 through 14 between the experimental results and the calculation is good. The failure of the model with respect to the energy dependence of the cross section for vector exchange shows most strongly in the production angular distributions but has a smaller effect on the density matrix elements. The absolute fits to the data are good evidence for the validity of the coupling constants used.

V. PRODUCTION AND DECAY OF $K^*(1400)^{0,-}$

A. $K^*(1400)$ Production

The $K^*(1400)^{0,-}$ is quite evident in the plots of Figs. 6 through 9. The resonance is seen to be produced with a substantial amount of nonresonant background. The uncertainties coming from this background is the primary source of error in determining the properties of this resonance.

To determine the mass and width of the $K^*(1400)$, each $K\pi$ invariant mass plot on Figs. 8 and 9 was fitted with a curve composed of phase space plus two Breit-Wigner functions with unknown central value and width. The results of these fits are given in Table IV. The best value for the mass of the $K^*(1400)$ is 1.416 ± 0.008 GeV. The width of the resonance is 0.089 ± 0.024 GeV in the K^{*-} charge state, while the K^{*0} appears to have a width of 0.173 ± 0.045 GeV. This latter value is probably distorted by the presence of misidentified events; when less restrictive cuts were used to select events of the final state $K^-\pi^+n$, the $K^*(1400)^0$ width obtained was 0.124 GeV. The width of the $K^*(1400)^-$ at 4.1 GeV/c could not be determined by fitting because of insufficient number of events. The values obtained for the $K^*(890)^{0,-}$ mass and width are in good agreement with previous determinations,¹⁰ except for the

TABLE IV. $K\pi N$ fits to phase space plus Breit-Wigner functions.

	$K^-\pi^+n$		$\bar{K}^0\pi^-p$	
	4.1 GeV/c	5.5 GeV/c	4.1 GeV/c	5.5 GeV/c
$K^*(890)$ mass (GeV)	0.896 ± 0.004	0.903 ± 0.004	0.896 ± 0.004	0.892 ± 0.002
$K^*(890)$ width (GeV)	0.053 ± 0.011	0.051 ± 0.011	0.041 ± 0.008	0.047 ± 0.004
$K^*(1400)$ mass (GeV)	1.405 ± 0.018	1.397 ± 0.019	1.401 ± 0.020	1.427 ± 0.009
$K^*(1400)$ width (GeV)	0.193 ± 0.065	0.152 ± 0.062	Fixed, 0.100	0.089 ± 0.024
Degrees of freedom	66	87	67	87
χ^2	59	92	72	80

mass of the $K^*(890)^0$ at 5.5 GeV/c, which is shifted up by about $1\frac{1}{2}$ standard deviations.

To study the $K^*(1400)^-$ angular distributions, only events of the two-prong-plus- V topology were used. For the study of the $K^*(1400)^0$, all fits to the final state $K^-\pi^+n$ which had χ^2 probability greater than 5% and which satisfied bubble-density estimates were used. The contamination of the $K^-\pi^+n$ final state from misidentified events in the $K^*(1400)$ region is much diminished when a selection is made on peripherally produced events as seen in Fig. 4.

The production angular distribution of the $K^*(1400)$ is shown in Fig. 17. Events with $K\pi$ invariant mass between 1.30 and 1.50 GeV were selected as containing the resonance, and the events used for background subtraction were those with $1.20 < M(K\pi) < 1.30$ GeV and $1.50 < M(K\pi) < 1.60$ GeV. The background is seen to be about 50% for each charge state at each energy.

The most striking feature of Fig. 17 is the difference between the distributions for $K^*(1400)^0$ and $K^*(1400)^-$ production. The K^{*0} is produced much more peripherally than is the K^{*-} . The same pattern was observed for the production of $K^*(890)^0$, where it was shown that π exchange in the production of K^{*0} and ω exchange in the production of K^{*-} were responsible for this behavior.

Hogaasen *et al.*²⁴ have investigated the predictions of the absorptive peripheral model for production of 2^+ mesons and have found that for vector-exchange processes both the production angular distribution and the absolute magnitude of the cross section, as well as the energy dependence, are incorrectly given, while for π exchange the shape of the angular distribution was approximately correct but the total cross sections were too large. We have found similar difficulties with the model and no reasonable fits were obtained for $K^*(1400)$ production. Thus, without a workable model, no definite conclusions can be made concerning the exchanged particles for $K^*(1400)^0$ production, although if one-particle exchange is assumed then it would appear that K^{*0} is produced by exchange of a lighter particle than for K^{*-} production.

B. $K^*(1400)$ Decay Angular Distributions

As discussed previously, the decay angular distributions of a resonance can be expressed in terms of the

²⁴ H. Hogaasen, J. Hogaasen, R. Keyser, and B. E. Y. Svensson, Nuovo Cimento 42, 323 (1966).

spin-density matrix elements which describe the polarization of the resonance. The functional dependence of this expression upon the density matrix elements is determined only by the spin of the resonance, while the value of each matrix element in the expression is determined by the resonance production mechanism. An analysis of decay angular distributions for the $K^*(1400)$ can therefore be made in a manner similar to that for the $K^*(890)$, except that the analysis must be made several times using each of the appropriate functional dependences for the possible spins of the resonance. Maximum-likelihood techniques then permits one to decide from this analysis which spin is most likely.

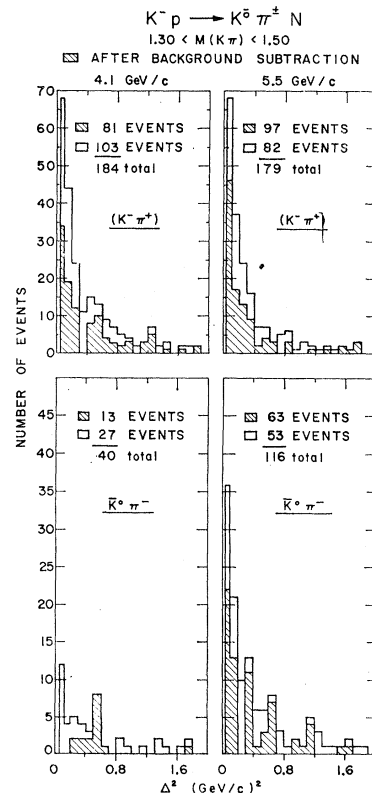


Fig. 17. $K^*(1400)^0$ production angular distribution in the reaction $K^-p \rightarrow K^*(1400)^0 N$. All events with $1.30 < M(K\pi) < 1.50$ GeV are selected as contributing to the resonance. The shaded areas represent the events remaining after background subtraction. The background is selected with $K\pi$ mass in the ranges 1.20 to 1.30 GeV and 1.50 to 1.60 GeV.

From the observed $K\pi$ decay, the $K^*(1400)$ must have natural parity (i.e., $J^P=0^+, 1^-, 2^+\dots$), and the decay into $K\pi\pi$ excludes 0^+ . Spins higher than 2 have been found to be unlikely,⁷ and in this experiment we investigate the possibility of spin-parity assignments 1^- and 2^+ . Previous results have shown 2^+ to be favored.^{7,8}

The decay angular distribution expected for a 1^- resonance is

$$W_1(\theta, \phi) = (3/4\pi) [\rho_{00} \cos^2\theta + \frac{1}{2}(1 - \rho_{00}) \sin^2\theta - \rho_{1,-1} \sin^2\theta \cos 2\phi].$$

For a 2^+ resonance produced by pseudoscalar- or vector-meson exchange the expected distribution is

$$W_2(\theta, \phi) = (15/16\pi) \{ 3\rho_{00}(\cos^2\theta - \frac{1}{3})^2 + 4 \sin^2\theta \cos^2\theta [\frac{1}{2}(1 - \rho_{00}) - \rho_{1,-1} \cos 2\phi] \}.$$

We have assumed that $\text{Re}\rho_{10}$ is zero, consistent with the absence in the exchange process of particles with spin greater than zero and with unnatural spin parity, and also that ρ_{ij} is zero if i or $j=2$, consistent with the exchange of particles with spins ≤ 1 . $\text{Re}\rho_{10}$ does become nonzero when absorption is present, but this effect is small as shown in Figs. 13 and 14.

For each of the distributions W_1 and W_2 the density-matrix elements were determined by the maximum-

likelihood method with the likelihood L defined as

$$\ln L = \sum_{i=1}^N \ln W(\theta_i, \phi_i) - \sum_{j=1}^M \ln W(\theta_j, \phi_j),$$

where i refers to the events with $K\pi$ mass between 1.30 and 1.50 GeV and j refers to the background events with $K\pi$ mass between 1.20 and 1.30 or 1.50 and 1.60 GeV. Each of the four groups of events shown in Fig. 17 was analyzed in this way using all $K^*(1400)$ events with $|t| < 2.0$ (GeV/c)². The distributions in $\cos\theta$ and ϕ for these events are shown in Figs. 18 and 19. The necessary

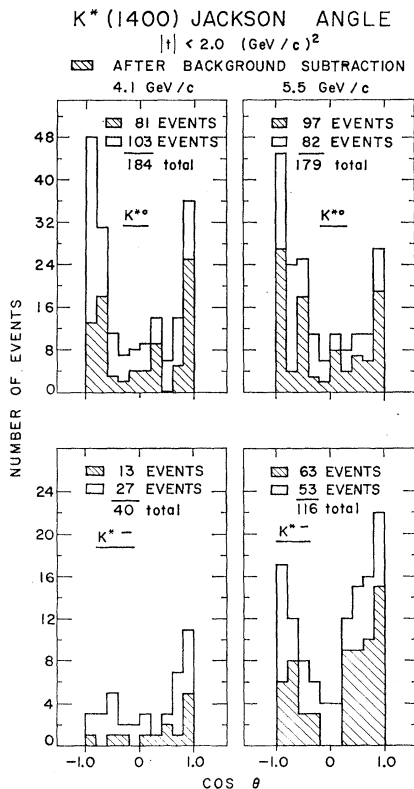


FIG. 18. Polar angles (Jackson angle, $\cos\theta$) distributions for the $K^*(1400)$ events shown in Fig. 17 with a four-momentum-transfer selection of $\Delta^2(N) < 2.0$ (GeV/c)².

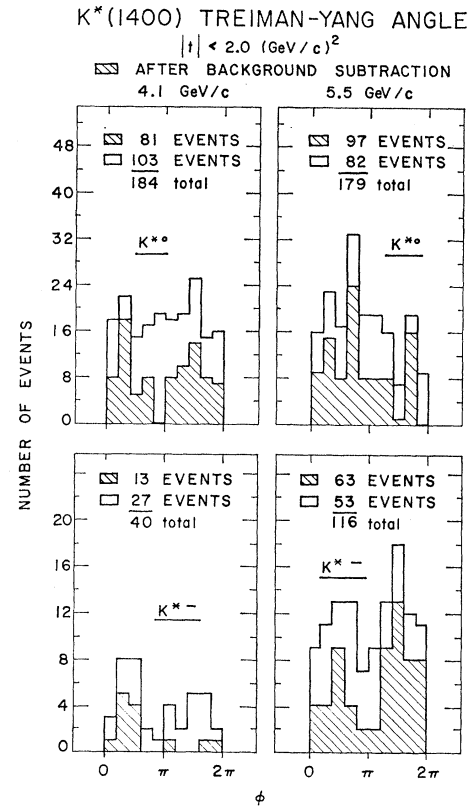


FIG. 19. Azimuthal angle (Treiman-Yang angle, ϕ) distributions for the $K^*(1400)$ events shown in Fig. 17 with a four-momentum-transfer selection of $\Delta^2(N) < 2.0$ (GeV/c)².

symmetries appear to be satisfied within statistical uncertainties except for K^{*-} at 5.5 GeV/c.

To compare the relative likelihoods of spin parity 1^- or 2^+ we define a ratio $R: R = \ln(L_2/L_1)$, where L_1 and L_2 are the likelihoods, L , for the two distributions W_1 and W_2 , using the best-fit values for the density matrix elements. The expected values of R can be calculated for each of the spin-parity assignments 1^- and 2^+ , and these expected values can then be compared with the experimentally determined value. This method of comparison was used by Haque *et al.*⁷ for analysis of $K^*(1400)^-$ produced in the reaction $K^-p \rightarrow \bar{K}^0\pi^-p$ at

TABLE V. $K^*(1400)^{0,-}$ spin-density matrix elements.

Events	1 ⁻ results		2 ⁺ results		$R = \ln(L_{2^+}/L_{1^-})$		
	ρ_{00}	$\rho_{1,-1}$	ρ_{00}	$\rho_{1,-1}$	Expected for 1 ⁻	Expected for 2 ⁺	Observed
$K^*(1400)^-, 4.1 \text{ GeV}/c$	$1.00_{-0.10}^{+0.00}$	$0.00_{-0.05}^{+0.05}$	$0.60_{-0.35}^{+0.20}$	$0.04_{-0.04}^{+0.12}$	-2.6	5.9	-1.8 ± 16.0
$K^*(1400)^-, 5.5 \text{ GeV}/c$	$0.80_{-0.10}^{+0.10}$	$0.10_{-0.05}^{+0.05}$	$0.00_{-0.00}^{+0.02}$	$0.25_{-0.25}^{+0.25}$	-16.5	12.8	1.9 ± 19.0
$K^*(1400)^0, 4.1 \text{ GeV}/c$	$0.80_{-0.10}^{+0.10}$	$0.10_{-0.05}^{+0.05}$	$0.80_{-0.10}^{+0.10}$	$0.10_{-0.05}^{+0.05}$	-21.0	21.1	5.7 ± 21.0
$K^*(1400)^0, 5.5 \text{ GeV}/c$	$0.80_{-0.15}^{+0.10}$	$0.05_{-0.05}^{+0.05}$	$0.50_{-0.10}^{+0.10}$	$0.15_{-0.10}^{+0.10}$	-5.8	5.7	2.1 ± 14.0

3.5 GeV/c, and the results showed a 2⁺ assignment to be favored over 1⁻ by about 2 standard deviations.

The results of our analysis are given in Table V. In general, we see that for our data the method is quite inconclusive. The basic problem is that the freedom given to each function W_1 and W_2 by permitting the density matrix elements to vary allows both functions to fit the data almost equally well, and only if there were many more events in the sample would the functional differences be able to distinguish between spin-parity assignments. For three of the four $K^*(1400)$ samples 2⁺ is slightly favored over 1⁻ but no decisive determination is obtained.

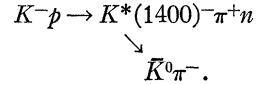
The production angular distributions of Fig. 17 may be used as an additional aid in considering spin-parity assignments. These distributions suggest that $K^*(1400)^0$ is produced by the exchange of a lighter particle than for $K^*(1400)^-$. The density matrix elements given in Table V show this is expected for 2⁺ but not for 1⁻.

Goldberg *et al.*²⁵ used the $K^*(1400)^{0,-}$ production angular distributions and the restrictions on ρ_{00} in a quantitative manner to make a spin-parity determination. Their results favor 2⁺ very strongly, but the distorting effects which absorption may have on the values of the density matrix elements, and the fact that the peripheral model has not yet successfully described the $K^*(1400)^{0,-}$ production distributions are weak points in their model-dependent analysis. In addition the weak $K\omega$ decay of the $K^*(1400)$ is difficult to reconcile with a production mechanism dominated by ω exchange. All of the above evidence suggests that the $K^*(1400)$ spin-parity assignment is 2⁺, but we conclude that without a satisfactory model for the production mechanism we cannot rule out other possibilities.

C. $K^*(1400)$ Decay Branching Ratios

Figure 20 shows the $K\pi$ and $\pi\pi$ mass distributions from the final state $\bar{K}^0\pi^+\pi^-n$. The $K^*(890)$ is very strongly produced at both energies with a background of $\sim 25\%$. The events shaded have a four-momentum transfer to neutron $< 1.0 \text{ (GeV}/c)^2$. In addition there is some evidence for $K^*(1400)$ production at 5.5 GeV/c with decay to $\bar{K}^0\pi^-$. We find a cross section of $36.3 \mu\text{b}$

for the reaction



The $\pi\pi$ mass distributions show clear evidence for ρ production over a large background.

The $\bar{K}^0\pi^-\pi^0$ invariant mass distribution from the final state $\bar{K}^0\pi^-\pi^0p$ is shown in Fig. 21. A large peak is observed in the $K\pi\pi$ mass region from 1.20 to 1.60 GeV which cannot be explained by a combination of known resonances. The $K^*(1400)$ resonance decaying into $K\pi\pi$ makes a contribution to this enhancement, but the total effect is too wide to be caused by the $K^*(1400)$ alone. Contributions to the $K\pi\pi$ enhancement may come from some of the reported resonances discussed by Bishop *et al.*²⁶ Other effects which will cause an enhancement in

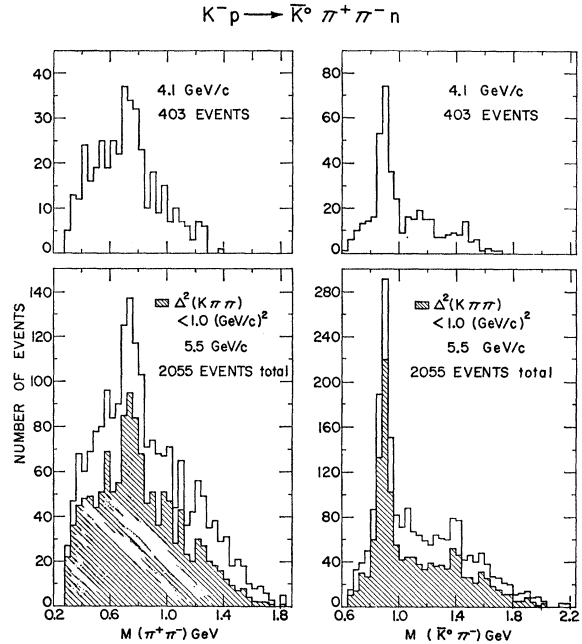


FIG. 20. $K\pi$ and $\pi\pi$ mass distributions from the reaction $K^-p \rightarrow \bar{K}^0\pi^+\pi^-n$ at 4.1 and 5.5 GeV/c. At both energies clear signals are observed for ρ^0 and $K^*(890)^-$ production. The shaded area at 5.5 GeV/c represents the events with a four-momentum transfer to the neutron $< 1.0 \text{ (GeV}/c)^2$. This selection is used in measuring the $K^*(1400)$ decay branching ratios.

²⁵ M. Goldberg, B. Goz, J. Leitner, V. Barnes, P. Dornan, G. Kalbfleisch, and I. Skillicorn, Phys. Rev. Letters **18**, 680 (1967).

²⁶ J. M. Bishop, A. T. Goshaw, A. R. Erwin, M. A. Thompson, W. D. Walker, and A. Weinberg, Phys. Rev. Letters **16**, 1069 (1966).

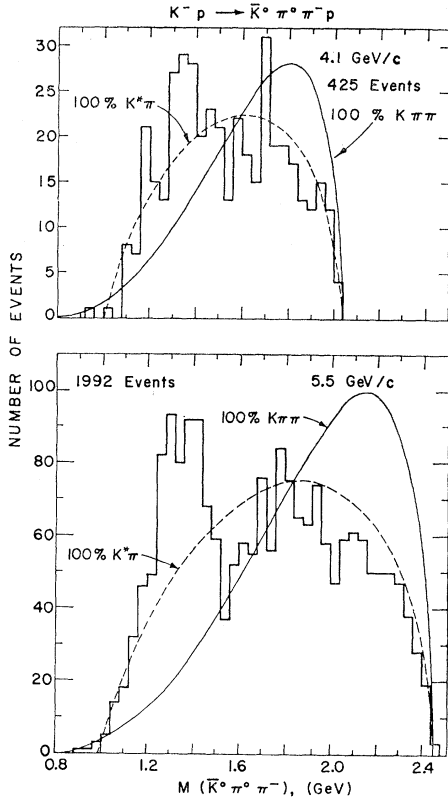


FIG. 21. $\bar{K}^0\pi^0\pi^-$ invariant mass distributions for the final state $\bar{K}^0\pi^0\pi^-p$ for 425 events at 4.1 GeV/c and 1992 events at 5.5 GeV/c. The solid curves are the distributions expected if the particles were distributed according to phase space with no resonances in the final state, and the dashed curves are the distributions expected if the production were entirely through the intermediate state $K^*(890)^0 \rightarrow \pi^-\pi^0 p$. The data shows a strong mass peak between 1.2 and 1.6 GeV.

the low $K\pi\pi$ mass regions are kinematic processes such as the Deck²⁷ effect or other diffractive dissociation processes. All these involve elastic diffraction scattering of the "exchange" particle by the target proton and therefore the effects are expected to be small in interactions in which charge exchange occurs at the baryon vertex. A detailed analysis of this proton final state will be presented in a later publication.

Figure 22 shows the $\bar{K}^0\pi^+\pi^-$ invariant mass distributions from the final state $\bar{K}^0\pi^+\pi^-n$. The large enhancements in the low $(K\pi\pi)^-$ mass region for the proton channel do not appear in the $(K\pi\pi)^0$ mass distributions. Peaks near 1.40 GeV are observed at both momenta. The shaded events in Fig. 22 are those with $\Delta^2(n) < 1.0$ (GeV/c)². This cut was made to purify the $K^*(1400)$ sample at 5.5 GeV/c. The dashed curves at each momenta show the Breit-Wigner resonance functions and backgrounds estimated to contribute to this region and used to determine the total $K\pi\pi$ contribution to $K^*(1400)$ decay. The resonance functions used had a width of 0.100 GeV and were centered at 1.440 and

²⁷ R. T. Deck, Phys. Rev. Letters **13**, 169 (1964).

1.400 GeV for 4.1 and 5.5 GeV/c beam momentum, respectively.²⁸ A comparison of these events with the $K^-\pi^+$ decay shown in Fig. 8 gives the ratio

$$\begin{aligned} (K^*(1400)^0 \rightarrow \bar{K}^0\pi^+\pi^-) / (K^*(1400)^0 \rightarrow K^-\pi^+) \\ = 0.49 \pm 0.10. \end{aligned}$$

Detailed results are given in Table VI.

Figure 23 shows the $K\pi\pi$ mass distributions when selections are made on the $K\pi$ mass or $\pi\pi$ mass. The cuts used to select samples of the $K^*(890)$ and ρ resonances were $0.842 \text{ GeV} < M(K\pi) < 0.942 \text{ GeV}$ and $0.630 \text{ GeV} < M(\pi\pi) < 0.910 \text{ GeV}$, with background selections of equal width on either side of the resonances (Fig. 20).

At 5.5 GeV/c only events with a four-momentum transfer to the neutron < 1.0 (GeV/c)² are used. The shaded events in Fig. 23 represent the data after background subtraction. In each case, peaks can be seen in the 1.4-GeV mass region. This procedure assumes the fraction of $K^*(890)$ and ρ in the background varies smoothly with $K\pi\pi$ mass. Since the $K^*(890)$ and ρ bands overlap on the $K\pi\pi$ Dalitz plot the data shown in

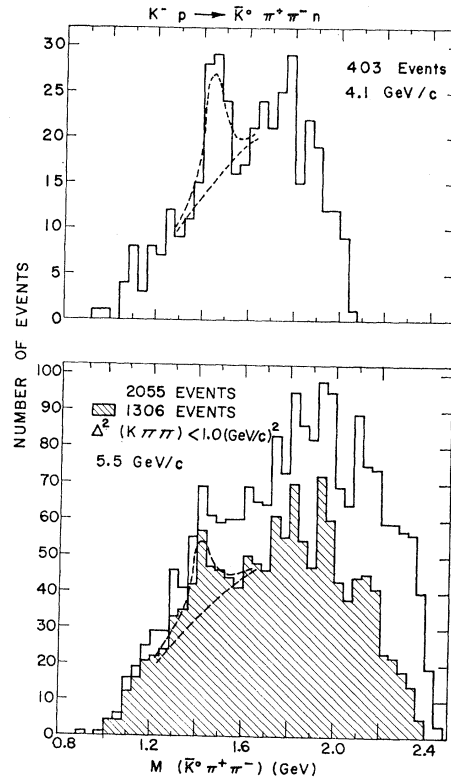


FIG. 22. $\bar{K}^0\pi^+\pi^-$ invariant mass distributions for the final state $\bar{K}^0\pi^+\pi^-n$ for 403 events at 4.1 GeV/c and 2055 events at 5.5 GeV/c. The shaded area at 5.5 GeV/c represents the events with a four-momentum transfer to the neutron < 1.0 (GeV/c)². The $K^*(1400)$ decaying into $(K\pi\pi)^-$ is evident at both momenta. The dotted lines show the estimated background and signal for this resonance.

²⁸ For $K^*(1400)$ decay to $K^*(890)\pi$ we expect a mass shift of ~ 5 MeV compared to the $K\pi$ decay because of the d -wave barrier.

Fig. 23 cannot be used on its own to give the decay branching ratios to $K^*\pi$ and $K\rho$.

Figure 24 shows the Dalitz plots for three $K\pi\pi$ mass selections representing the $K^*(1400)$ resonance and neighboring regions; to show the background behavior. The $K^*(890)$ band is seen on all the Dalitz plots but a ρ region enhancement is not so clear. Using the Dalitz plots of Fig. 24 to give the $K^*\rho$ overlap region, the mass peaks of Fig. 23 measure the $K^*(1400)$ decay to $K^*\pi$ and $K\rho$. The data was also analyzed using the Dalitz-plot information alone. The results are summarized in Table VI and compared to the $SU(3)$ predictions of Goldberg *et al.*²⁹ The predictions are in reasonable accord with our experimental results.

VI. SUMMARY OF RESULTS

The reaction $K^-p \rightarrow K\pi N$ at 4.1 and 5.5 GeV/c are dominated by the production of K^* resonances. $K^*(890)$ is the most prominent of these, representing 27 to 47% of the events, and $K^*(1400)$ is also quite evident, accounting for 12 to 16% of the events. The K^* resonances are produced strongly peaked forward in the center-of-mass frame, and no appreciable production above a very low background is observed in the backward direction.

The most striking difference between the results at 4.1 and 5.5 GeV/c is the decrease in production cross sections with increase in energy. At 5.5 GeV/c the K^* production cross sections are about 60% of those measured at 4.1 GeV/c. The cross sections for the total $K\pi n$ state are found to decrease at about the same rate as for K^* production, so that the fraction of K^* events is unchanged with the change in energy. The change in production and decay angular distributions in going from 4.1 to 5.5 GeV/c is very small.

TABLE VI. $K^*(1400)^0$ decay branching ratios, and comparison with $SU(3)$ predictions.

$K^- + p \rightarrow$ $K^*(1400)^0 + n$	Number of events		Cross section (μb)	
	4.1 GeV/c	5.5 GeV/c ^a	4.1 GeV/c	5.5 GeV/c
$\bar{K}^0\pi^+\pi^-$ total	36 ± 8	66 ± 10	119 ± 26	48 ± 9
$K^*(890)^-\pi^+$				
$\bar{K}^0\pi^-$	25 ± 6	46 ± 10	83 ± 20	33 ± 5
$\bar{K}^0\rho^0$	11 ± 8	15 ± 8	36 ± 27	11 ± 8
$\bar{K}^0\pi^+\pi^-$	< 10	< 10	< 33	< 10
Decay branching ratio	4.1 GeV/c	5.5 GeV/c	Mean	$SU(3)$ prediction
$K^*\pi/K\pi$	0.59 ± 0.15	0.44 ± 0.15	0.52 ± 0.12	0.67
$\bar{K}\rho/K\pi$	0.34 ± 0.27	0.19 ± 0.17	0.26 ± 0.16	0.17

^a $\Delta^2(n) < 1.0$ (GeV/c)².

²⁹ M. Goldberg, J. Leitner, R. Musto, and L. O'Raifeartaigh, Nuovo Cimento 45, 169 (1966).

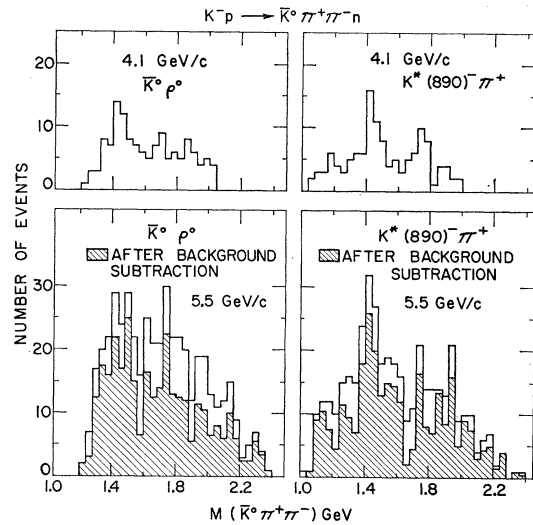


FIG. 23. Evidence for the decay of $K^*(1400)$ into $K^*(890)\pi$ and $K\rho$. The $\bar{K}^0\pi^+\pi^-$ mass is plotted for events which contain a $K^*(890)$ or a ρ . The shaded area represents the events remaining after background subtraction. In all cases peaks can be seen in the 1400-MeV mass region.

Production of $N^*(1236)$ accounts for 2% to 8% of the events in the $K\pi N$ final states. The cross sections and energy dependence for $N^*(1236)$ production are found to be in quite reasonable agreement with the predictions of the Regge-pole model of Arnold.

For both $K^*(890)^0-$ and $K^*(1400)^0-$ production, the K^*0 is peaked more sharply forward than is the K^*- . This suggests that a lighter particle is exchanged in the production of the neutral resonance. For $K^*(1400)^0-$

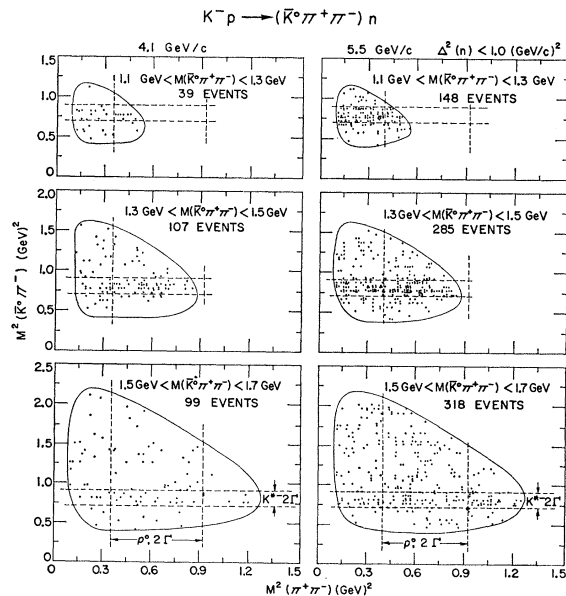


FIG. 24. Dalitz plots of the $K\pi\pi$ system with mass selections to specify the region of the $K^*(1400)$ resonance and neighboring mass bands.

production the absorptive peripheral model gives no reasonable results, but for $K^*(890)^{0,-}$ production the exchange mechanism can be determined using the model. The results agree well with the observed $K^*(890)^{0,-}$ production and decay angular distributions. Pion exchange is the dominant mechanism in production of $K^*(890)^0$ while ω exchange is dominant for $K^*(890)^-$ production.

The $K^*(1400)^{0,-}$ production and decay angular distributions suggest that the spin parity of the $K^*(1400)$ is 2^+ , but without many more events or a better model for the production mechanism we cannot make a decisive determination. A better theoretical model would permit a quantitative use of the production angular distributions for $K^*(1400)^0$ and $K^*(1400)^-$ to help determine the spin-density matrix elements. This would then place more restrictions on the decay angular corre-

lations so that a more definite distinction could be made between the distributions expected for different spin states.

The $K^*(1400)^0$ decay into $K\pi\pi$ appears to proceed entirely through $K^*(890)\pi$ and $K\rho$. The rates observed are in agreement with the $SU(3)$ predictions which assume that the $K^*(1400)$ is a member of a 2^+ octet.

ACKNOWLEDGMENTS

The experiment was made possible by the participation of our colleagues at the Universities of Illinois and Wisconsin in the design, construction, and operation of the separated beam. In addition we wish to thank the ZGS and 30-in. bubble chamber staff for cooperation under conditions which were often difficult. Finally we thank our scanners both at Argonne and Northwestern for their careful work over an extended period.

Positron-Proton Elastic Scattering at 800 and 1200 MeV*

R. L. ANDERSON,† B. BORGIA,‡ G. L. CASSIDAY, J. W. DEWIRE, A. S. ITO, AND E. C. LOH

Laboratory of Nuclear Studies, Cornell University, Ithaca, New York

(Received 15 September 1967)

The cross section for the elastic scattering of positrons from protons has been compared with the corresponding electron cross section using secondary beams derived from the photon beam of the Cornell 2-GeV synchrotron. The paths of the scattered leptons (positrons or electrons) and recoil protons were recorded in spark chambers and were used to determine the incident lepton energy of each event. Elastic scatterings were identified by requiring coplanarity and a fit to the scattering kinematics. The detection system was sensitive to scattering angles between 25° and 75° . The ratio of the positron cross section to the corresponding electron cross section was 0.992 ± 0.017 at 800 MeV and 0.987 ± 0.019 at 1200 MeV. No significant variation of the ratio with angle of scattering was found.

INTRODUCTION

A COMPARISON of the elastic scattering of positrons from protons with the well-known electron-proton process could be a sensitive test for the presence of two-photon exchanges in the interaction. At present, the large quantity of data on the absolute cross section for electron-proton scattering can be understood in terms of only single-photon exchanges, which lead to the Rosenbluth formula¹ for the scattering cross section. While it is true that the exchange of more than one photon should lead to a deviation from the Rosenbluth formula, the detection of such a deviation is made difficult by the need to make accurate absolute cross sections for comparison with the theory. The most

accurate test of the well-known $\cot^2(\frac{1}{2}\theta)$ dependence of the scattering cross section, predicted by the Rosenbluth formula, is in excellent agreement with the theory.² A direct comparison of the positron-proton and electron-proton scattering rates for identical kinematic limitations is not subject to some systematic errors associated with absolute determinations. Furthermore, interference terms between one- and two-photon exchange processes, which depend on the sign of the leptonic charge, have an effect on the ratio of cross sections which is twice the effect on each cross section.

Two-photon exchange processes may also produce a linear polarization of the recoil proton, but the degree of polarization is proportional to the imaginary part of the amplitude for two-photon exchange while the contribution to the cross section comes from the real part of the amplitude. Experimental measurements have

* Supported in part by the U. S. Office of Naval Research and the National Science Foundation.

† Present address: Stanford Linear Accelerator Laboratory, Stanford, Calif.

‡ Present address: Istituto di Fisica, Universita di Roma, Rome, Italy.

¹ M. N. Rosenbluth, Phys. Rev. **79**, 615 (1950).

² W. Albrecht, H. J. Behrend, F. W. Brasse, W. Flauger, H. Hultschig, and K. G. Steffen, Phys. Rev. Letters **17**, 1192 (1966).